

An Iterative-Mode Scan Design of Terrestrial Laser Scanning in Forests for Minimizing Occlusion Effects

Linyuan Li^{ID}, Associate Member, IEEE, Xihan Mu^{ID}, Maxime Soma, Peng Wan, Jianbo Qi, Ronghai Hu^{ID},
Wuming Zhang^{ID}, Yiyi Tong^{ID}, and Guangjian Yan^{ID}, Senior Member, IEEE

Abstract—Occlusion effect, an inherent problem of terrestrial laser scanning (TLS) measurements, limits the potential of TLS data in tree attribute estimation. Multiple scans seek to mitigate this effect to provide enhanced scan completeness. However, the numbers and locations of the scans (i.e., the scan design) are usually determined via a subjective assessment of the tree density, spatial patterns of trees, and attributes to be derived. These could cause suboptimal scan completeness and limit tree attribute estimation. This study proposed an iterative-mode scan design to minimize the occlusion effect. First, we introduced a PoTo index based on visibility analysis to evaluate how many trees can be scanned from a location and to select effective candidates for the optimal TLS location. Second, we introduced a cumulative degree of ring closure (CDRC) to quantify the scan completeness for each candidate and determine the optimal TLS location. The TLS data sets of virtual forests with field-measured and synthetic plot parameter settings were simulated according to iterative- and regular-mode designs by using a Heidelberg light detection and ranging (LiDAR) Operations Simulator (HELIOS). The results demonstrated that an iterative-mode design can improve the scan completeness of trees compared to the regular-mode design. The tree attribute (diameter at breast height (DBH), tree height, stem curve, and crown volume) estimates of the iterative-mode design were less erroneous than those of the regular-mode design (e.g., the root-mean-square error (RMSE) could decrease the stem curve estimation by 38% and the crown volume estimation by 15%). This study suggests that the iterative-mode design can obtain an improved quality of the TLS data, especially for dense stands.

Index Terms—Forest inventory, occlusion effect, scan design, terrestrial laser scanning (TLS), tree attributes, visibility analysis.

I. INTRODUCTION

TERRESTRIAL laser scanning (TLS), also known as ground-based light detection and ranging (LiDAR), is a powerful tool for quantifying 3-D forest structures with unprecedented levels of detail and geometric accuracy [1], [2]. The terrestrial platforms, compared with airborne and spaceborne platforms, allow comprehensive beam coverage of the area of interest [3]. Terrestrial LiDAR facilitates detailed forest modeling [4] and the quantification of tree attributes [5]–[7], e.g., stem curve, stem volume, biomass, and leaf area density. Highly detailed forest measurements also serve as references for validating the retrieval variables from airborne and spaceborne platforms [8] and for simulating radiative transfer within the forest canopy [4].

However, various field conditions can affect the quality and characteristics of the TLS point cloud data [2], [9], [10]. These conditions generally include the weather (e.g., wind and fog) and forest (e.g., tree density, architecture, and species) [3], of which complex forest structure induces an occlusion effect by shading other objects in the direction of the laser propagation. The occlusion causes unobserved volumes and missing elements, which limit the potential of TLS and lead to uncertainty in the tree attribute measurements [11]–[13].

Single- and multiscan approaches have been reported for the data acquisition of a single plot. Previous studies have shown that up to 40% of all the trees in a sample plot might not be detectable with a single scan from the plot center in the single-scan approach, [12], [14], [15]. In the multiscan approach, scans are coregistered to merge information from various viewpoints. Hence, the multiscan approach has the potential to provide full coverage of the stem surface and is the most accurate technique for measuring forest plots [3]. Previous studies have identified that the occlusion effect can be largely eliminated by coregistering multiple scans [3], [16]. However, because general rules for determining the optimal scan design have not been established, the locations and numbers of multiple scans are usually decided by the operators [17], [18]. For example, the commonly used design (i.e., regular-mode design) is composed of a scan near the center with the other scans regularly distributed inside or outside the plot. This subjective decision could lead to suboptimal coverage and biased sampling of a targeted area, which cannot

Manuscript received January 20, 2020; revised July 7, 2020; accepted August 17, 2020. This work was supported in part by the National Natural Science Foundation of China under Grant 41871230 and Grant 41671414, in part by the China Scholarship Council under Grant 201706040156, and in part by the Institut National de la Recherche Agronomique (INRA) through UMT-CAPTE. (Corresponding author: Xihan Mu.)

Linyuan Li is with the State Key Laboratory of Remote Sensing Science, Faculty of Geographical Science, Beijing Normal University, Beijing 100875, China, and also with INRA EMMAH UMR1114, 84914 Avignon, France.

Xihan Mu, Yiyi Tong, and Guangjian Yan are with the State Key Laboratory of Remote Sensing Science, Faculty of Geographical Science, Beijing Normal University, Beijing 100875, China (e-mail: muxihan@bnu.edu.cn).

Maxime Soma is with INRAE EMMAH UMR1114, Avignon 84914, France.

Peng Wan is with the Changjiang River Scientific Research Institute (CRSRI), Wuhan 430010, China.

Jianbo Qi is with the Key Laboratory for Silviculture and Conservation of Ministry of Education, Beijing Forestry University, Beijing 100083, China.

Ronghai Hu is with the College of Resources and Environment, University of Chinese Academy of Sciences, Beijing 100049, China.

Wuming Zhang is with the School of Geospatial and Engineering Science, Sun Yat-sen University, Zhuhai 519082, China (e-mail: zhangwm25@mail.sysu.edu.cn).

Color versions of one or more of the figures in this article are available online at <http://ieeexplore.ieee.org>.

Digital Object Identifier 10.1109/TGRS.2020.3018643

be corrected afterward [19]. Increasing the number of scans allows for a reduction in the occlusion effect and achieves more complete data [10]. However, this process requires additional time for the field data acquisition [20], e.g., replacing the coregistration reflectors and moving all the equipment and scanners. Additionally, excessive scans imply great effort in data processing and storage. In particular, manual or semiautomated coregistration is a challenging work that requires clear tie points and complex computations. Therefore, arbitrarily configuring the number of scan locations without considering the practical situation of the occlusion effects in forest plots could cause redundant yet incomplete sampling in spite of high labor and time costs. This circumstance motivates the development of a scan design that considers the practical situation of occlusion effects and that has the potential to maximize the scan completeness and improve the TLS data quality.

Previous studies have demonstrated that the occlusion effect is highly related to the spatial pattern of the trees, the tree density, and tree size [15], [21]. The 2-D cross section of a 3-D forest retains the spatial pattern, tree density, and size regardless of the height information and 3-D shape, which provides the possibility of quantifying the occlusion effect in forest plots. Furthermore, the quantitative value of the occlusion effect can be an indicator for determining the optimal TLS locations. In this study, we developed a new scan design of the TLS locations, namely, iterative-mode design, by introducing the map of the tree locations and tree sizes because this map is available from various measurement methods [22], [23]. Quantitative indicators associated with the occlusion effect can be calculated based on the map and then used to derive the optimal TLS locations. The design aims at maximally mitigating the occlusion effect and achieving complete and low-redundant sampling through multiple scans. Importantly, this study will offer insights into the influence of the scan design on the scan completeness and tree attribute estimation (diameter at breast height (DBH), tree height, stem curve, and crown volume) based on the simulated TLS point clouds.

In this study, our main research questions are as follows: 1) How can optimal scan locations be designed to minimize the occlusion effect? 2) What are the performances of the proposed scan design on the scan completeness and tree attribute estimation? 3) What are the influences of the spatial pattern of trees, tree density, and tree size on the occlusion effect, optimal scan locations, and estimation accuracy?

II. METHODS

A. Iterative-Mode Scan Design

We assume that an individual tree can be represented by an enclosed circle in 2-D space. The tree circle diameter is assigned to either DBH or crown diameter, depending on different applications. For example, the tree circle diameter equals the DBH for stem mapping, whereas it equals the crown diameter for crown variable estimation (e.g., leaf area density).

The iterative-mode scan design is developed to optimize the numbers and locations of the TLS scans based on two aspects: 1) the number of trees that can be scanned from a

location and 2) the angular percentage of a tree scanned from a location. Correspondingly, we introduced an index, named the PoTo index, based on the visibility analysis to describe the percentage of the number of trees that can be scanned at a location in a given plot. We additionally introduced the cumulative degree of ring closure (CDRC) to assess the scan completeness of each tree for the locations in the iterative processes.

The proposed algorithm for the iterative-mode scan design consists of five main steps: 1) inputting a data table that contains the x - y coordinates of the centers and radii of the tree circles; 2) producing a PoTo index map of the forest plot; 3) selecting the effective candidates for the optimal TLS location; 4) determining the optimal TLS location; and 5) determining whether additional scans and iterations are needed. Each iteration contains these five steps. We developed a customized script package programmed in MATLAB R2018a (MathWorks, Inc., Natick, MA, USA) to implement the algorithm for the iterative-mode design. The step-by-step workflow is illustrated in Fig. 1 and is described next.

1) *Producing the PoTo Index Map*: The PoTo index of a location is defined as the percentage of the number of trees that can be scanned from this location [see (1)]. It is introduced to assess how many trees can be scanned from a TLS location

$$\emptyset_i(x, y) = V_i(x, y)/N_i \cdot 100\% \quad (1)$$

where $\emptyset_i(x, y)$ refers to the PoTo index of a location (x, y) in a plot in the i th iteration, $V_i(x, y)$ represents the number of tree circles that can be observed from the location (x, y) , and N_i is the total number of tree circles in the i th iteration and will be updated in each iteration. In the first iteration, N_i equals the total number of trees in the plot. In subsequent iterations, N_i is the total number of trees that need additional scans (see step 1 in Fig. 1). We used a visibility analysis method to calculate the PoTo index for all locations in the forest plot. Visibility analysis produces the areas (Fig. 2(a), green areas) that are visible to a location by calculating the interactions between the sightlines and objects [21], [24]–[26]. Appendix presents the detailed computation of the visibility analysis. In our implementation, instead of computing the visible areas observed from each location one by one, we computed the areas that were visible to each tree location and then produced the PoTo index map. First, we computed the visible areas to produce a visibility map for each tree location [Fig. 2(a)]. Each x - y coordinate within the visible areas [i.e., green areas, Fig. 2(a)] was assigned the value of 1, and the x - y coordinate within the invisible area was assigned 0. Second, the visibility maps for all tree locations were summed up into a global visibility map for the entire forest plot. Therefore, the value of an x - y coordinate in the global visibility map of the plot refers to how many times that coordinate can be observed from all tree locations. This is equivalent to how many trees can be observed from this coordinate according to the reciprocal rule. Third, the PoTo index map [Fig. 2(b)] was derived by dividing the visibility map of the plot with the total number of trees in the current iteration [see (1)].

The PoTo index map quantifies the occlusion effect of all spatial locations in the plot. Apparently, a high PoTo index

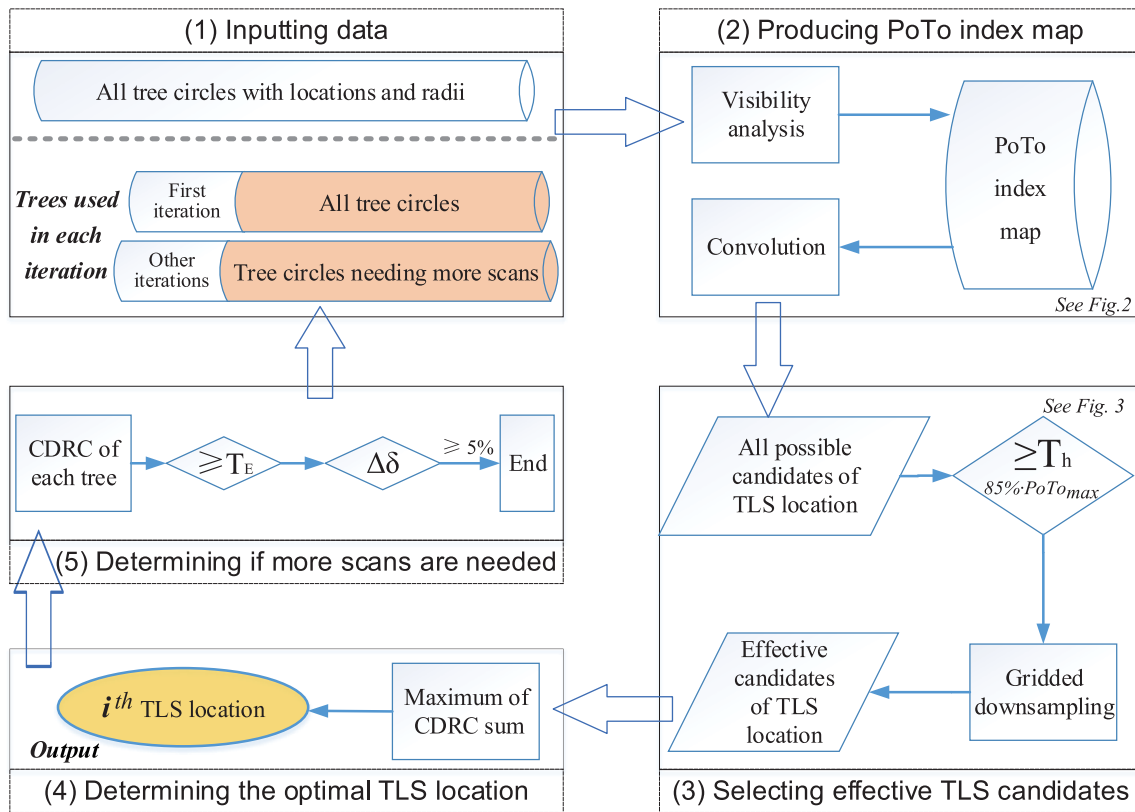


Fig. 1. Implementation of the iterative-mode scan design, where the scan time i equals $1, 2, \dots$, and the threshold T_h is defined as 85% of the maximum PoTo index. The threshold T_E refers to the expected CDRC set by the operator. Tree circles that need more scans change at each iteration. $\Delta\delta$ refers to the difference in the detection rate between the neighboring two iterations.

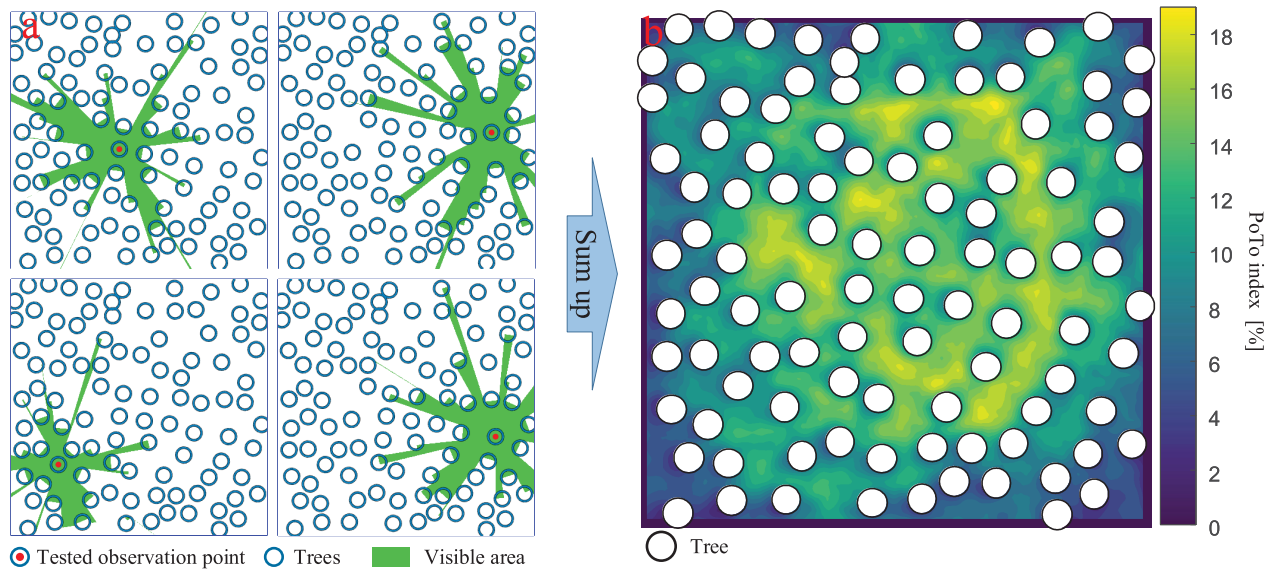


Fig. 2. Illustration of the visibility analysis method to produce a PoTo index map for a forest plot. (a) Four visibility maps derived from four different tree locations and (b) PoTo index map of this plot.

implies a low occlusion effect, whereas a low PoTo index indicates a high occlusion effect [Fig. 2(b)]. Furthermore, given that the high-PoTo-index values might be located in a small area where the neighboring areas have low-PoTo-index values, a convolution process was conducted onto the PoTo index map to alleviate this problem. The PoTo index map

serves as the base data to select the optimal TLS location and is updated in each iteration.

2) *Selecting the Effective Candidates for the TLS Location:* In an iteration, all the candidates of a TLS location were derived by extracting the high-PoTo-index positions via a specific threshold (T_h , i.e., 85% of the maximum PoTo index)

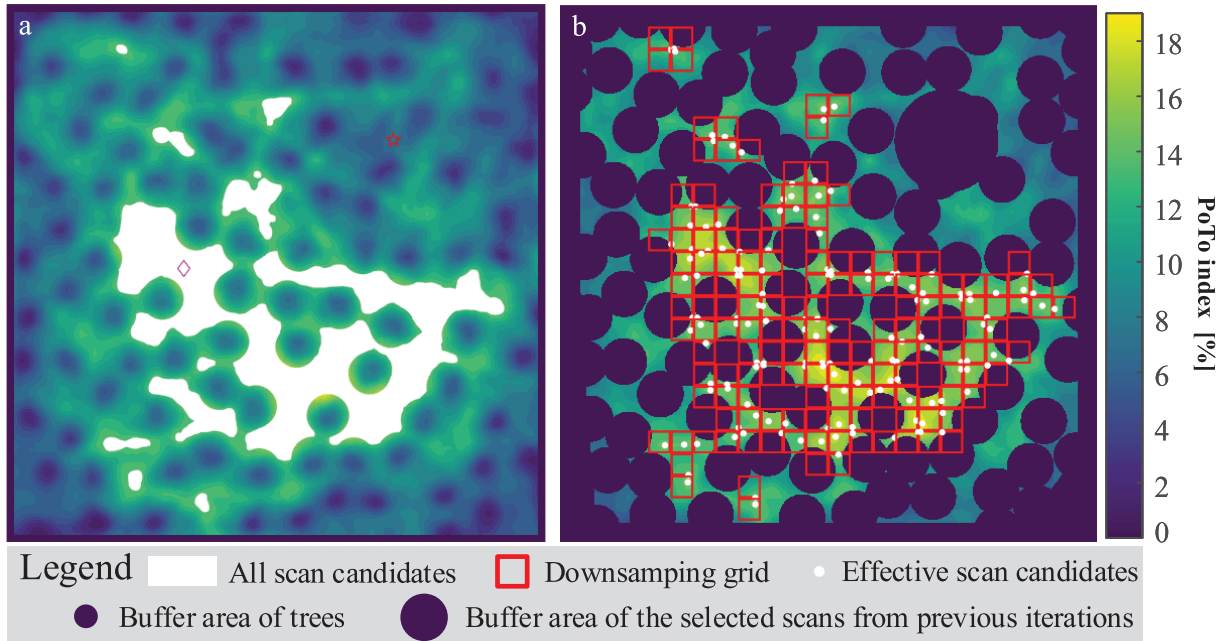


Fig. 3. Illustration of the gridded downsampling of all candidates for the optimal TLS location based on the PoTo index map. (a) Map of all TLS candidates. (b) Selection of the effective candidates of the optimal TLS location in each grid.

in the PoTo index map [Fig. 3(a)]. Considering that the adjacent locations have similar PoTo index values, we downsampled all the candidate locations by a gridded downsampling of the PoTo index map. Technically, a coarse grid array (cell width = 2 m) was created only for the regions of the candidates [red grids in Fig. 3(b)]. Only the candidate with the highest PoTo index value in each grid was reserved [white dots in Fig. 3(b)]. These reserved candidates were the effective candidates of the optimal TLS location for further processes.

Additionally, to avoid too close a distance between TLS and trees, we set a buffer area for each tree with 1.3 times the tree radius [small blue circles in Fig. 3(b)]. We also added a circle-shape buffer area (a radius of 5 m) for the optimal locations selected in previous iterations [the large blue circle in Fig. 3(b)]. This strategy has the potential of preventing too short of a distance among the scan locations, and it benefits maximization of the scan's completeness.

3) *Determining the Optimal TLS Location by CDRC*: The CDRC is defined as the angle of the union of scanned sectors for a tree circle (e.g., α_1^A and α_2^A in Fig. 4). The CDRC value is 0° when the circle is not scanned at all and equals 360° when the circle is completely scanned. The scan completeness of each effective candidate for the optimal TLS location was quantified through the proposed CDRC index; hence, this index can determine the optimal TLS location. The optimal TLS scan (x_{os}^i, y_{os}^i) is located at the position where the CDRC sum of all the tree circles reaches the maximum

$$(x_{os}^i, y_{os}^i) = \operatorname{argmax} \sum_{j=1}^{N_i} \alpha_j(x_{ec}^i, y_{ec}^i) \quad (2)$$

where i refers to the i th iteration, $\alpha_j(x_{ec}^i, y_{ec}^i)$ is the CDRC for the j th circle, and (x_{ec}^i, y_{ec}^i) refers to the location of the effective TLS scan candidate. The subscripts os and ec mean

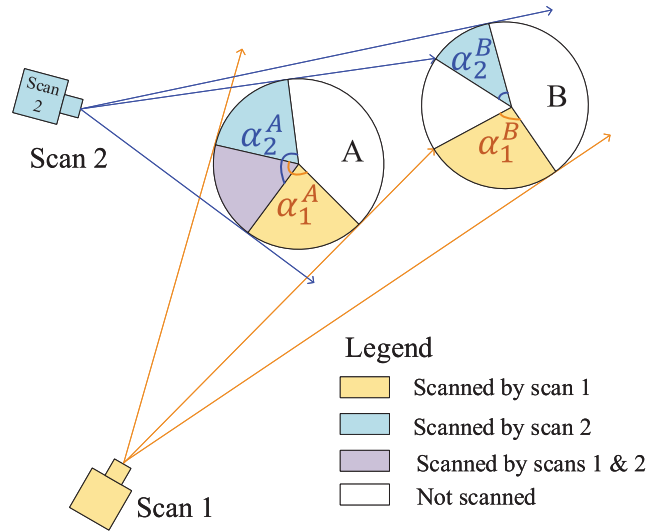


Fig. 4. Illustration of the CDRC of tree circles with two scans.

the optimal TLS location and the effective candidate of the optimal TLS location, respectively.

4) *Determining Additional Scans or Stop*: We used the detection rate (δ) as an indicator to stop running or continue iterations for additional TLS scans. It is defined as the percentage of the number of trees that meet the requirement of operator-expected CDRC (T_E) out of the number of all trees in the plot (N_{total}) [see (3)]. Note that $I(j)$ is an indicator function in (3). If the detection rate is larger than 95%, the program will stop, and the optimal TLS location in each iteration will be exported. If the difference in the detection rate between two adjacent iterations is less than 5% and detection rate is larger than 80%, the program will

also stop in consideration of the low contribution made by the subsequent scan; hence, all the optimal TLS locations will be outputted except for the one in the last iteration. Otherwise, new iterations will be conducted for additional scans

$$\delta = \sum_{j=1}^{N_{\text{total}}} I(j)/N_{\text{total}} \cdot 100\%, I(j) = \begin{cases} 1, & \text{CDRC}_j \geq T_E \\ 0, & \text{CDRC}_j < T_E. \end{cases} \quad (3)$$

It should be noted that T_E is an important parameter for the determination of stopping. If the CDRC of the j th tree circle (CDRC_j) reaches the T_E defined by the operator, then it is unnecessary to conduct additional sampling for this tree. Otherwise, further sampling is required for this tree. Note that the tree circles used in the new iteration (N_i) become the tree circles whose CDRC values are smaller than T_E . Correspondingly, the PoTo index map will be updated by summing up the visibility maps of these tree circles. In addition, the T_E value in the first iteration is usually different from the subsequent iterations, because the CDRC of trees in the first iteration is definitely less than 180° . The T_E is set to be a value less than 180° , e.g., 120° . For subsequent iterations, the CDRC of the trees can exceed 180° , and the T_E is, therefore, set to be a value larger than 180° , e.g., 200° . We also suggest setting a larger value for T_E for the forest plot with a larger average tree circle diameter and vice versa. In addition, the value of T_E also depends on the tree attributes to be derived.

B. Regular-Mode Scan Design

In the multiscan approach, the commonly used scan design (i.e., regular mode) is composed of a scan at the center and the other scans regularly distributed inside or outside the plot [2]. In field plots, the regular-mode designs of five-scan measurements included one scan at the center and the other four scans distributed at the four plot corners. If the scan location was overlapping with stems, the scan would be slightly shifted [20]. In synthetic plots, the regular-mode design consisted of four scans in the central region and four scans in the four corners of the plot, for eight-scan measurements. Given that dense scans distributed in systematic grids can achieve more complete coverage for all trees in the plot [3], the regular-mode design of 16-scan measurements contains four scans located in the central region and the remainder distributed along the plot borders (see Section IV-D).

III. MATERIALS

A. Forest Plots and Tree Models

Two data sets for the study were generated using field and synthetic plot parameter settings. The field plot parameters were derived from six public forest plots provided by the international TLS benchmarking project launched by the Finnish Geospatial Research Institute, Masala, Finland [27]. The corresponding data set was used to assess the performance of different scan designs on stem attribute retrieval when taking forest inventories. The use of this data set facilitated a comparison with previous studies (see [15]) in the framework of the benchmarking project. The synthetic plot parameters were

set based on three types of classical spatial distributions in a natural forest. The corresponding data set aims at assessing the performance of different scan designs on crown attribute estimation. The investigation using this data set is also valuable for fine forest reconstruction.

1) *Field Plot Parameter Settings*: The six public field plots were categorized into “easy,” “medium,” and “difficult” plots according to the complexity of the tree architecture (Table I). The stem visibility at ground level, stem density, and DBH distribution was considered in the complexity assessment. Earth surface of all plots is flat with a plot size of $32 \text{ m} \times 32 \text{ m}$ in a southern boreal forest in Evo, Finland (61.19° N , 25.11° E). The field plot parameters, including the tree location, height, and DBH, were collected by the integration of field inventories and manual measurements from the TLS data. For the details about these plots, please refer to the original article about the international TLS benchmarking project [27].

We used the field plot parameters and a basic broadleaf tree (*Betula pendula*) model [Fig. 5(a) and (b)] to generate six virtual forest scenarios, thus ensuring consistency with the field actual forest plots in terms of scene structures. The basic tree model was created by a 3-D realistic tree structure modeling software, OnyxTREE BROADLEAF 7.0, according to the exponential relationship between the tree height and DBH (Table I). The virtual forest scenarios were technically established by replicating the basic tree model and then transforming it (i.e., scale, translate, and rotate) according to the field tree location, tree height, and DBH [Fig. 6(a)–(f)]. The virtual forest models were resampled into point clouds with a resolution of 1 mm to serve as reference point clouds for the simulated TLS point clouds. In this data set, we parameterized each tree as a circle with the radius of its DBH in the scan design optimization.

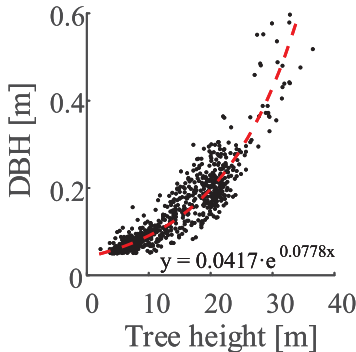
2) *Synthetic Plot Parameter Settings*: Three types of spatial patterns (i.e., random, row, and clumped) were used to establish the synthetic forest plots within the flat square ground surface ($50 \text{ m} \times 50 \text{ m}$). These patterns have the ability to represent various natural forests and plantations while characterizing different occlusion effects. In each spatial pattern, three plots with a specific number of trees were generated (Table I).

We used a fully grown broadleaf tree (*Betula pendula*) model [Fig. 5(c)] to generate different forest plot models according to the defined patterns. The tree height is 8.934 m, and the crown base height is 1.003 m. The trees within a plot were completely the same without any scale transformation. No overlapping among the trees occurs for random and row patterns, whereas slight overlapping among several tree crowns is observed for the clumped pattern [Fig. 6(g)–(i)]. The radius–height profile [Fig. 5(d)] shows that the maximum radius of the tree crown is almost 1.5 m. Thus, we parameterized the tree as a circle with a radius of 1.5 m in this data set.

B. TLS Data Simulation With HELIOS

The Heidelberg LiDAR Operations Simulator (HELIOS) provides a tool for simulating the multipulse data, especially

TABLE I
OVERVIEW OF DATA SETS WITH FIELD (“EASY,” “MEDIUM,” AND “DIFFICULT”) AND SYNTHETIC (RANDOM, ROW, AND CLUMPED) PLOT PARAMETER SETTINGS IN THIS STUDY

Category	Plot ID	Plot size	Tree count	Feature	Virtual forest generation	Purpose
Easy	1		51	Varying tree height		Stem attributes
	2		84			
Medium	3	32 ×	148			
	4	32 m ²	78			
Difficult	5		131			
	6		236			
Random	7~9	50 ×	99	Constant tree height	Tree height = 8.934 m Crown base height = 0.95 m	Crown attributes
Row	10~12	50 m ²	100			
Clumped	13~15		93			

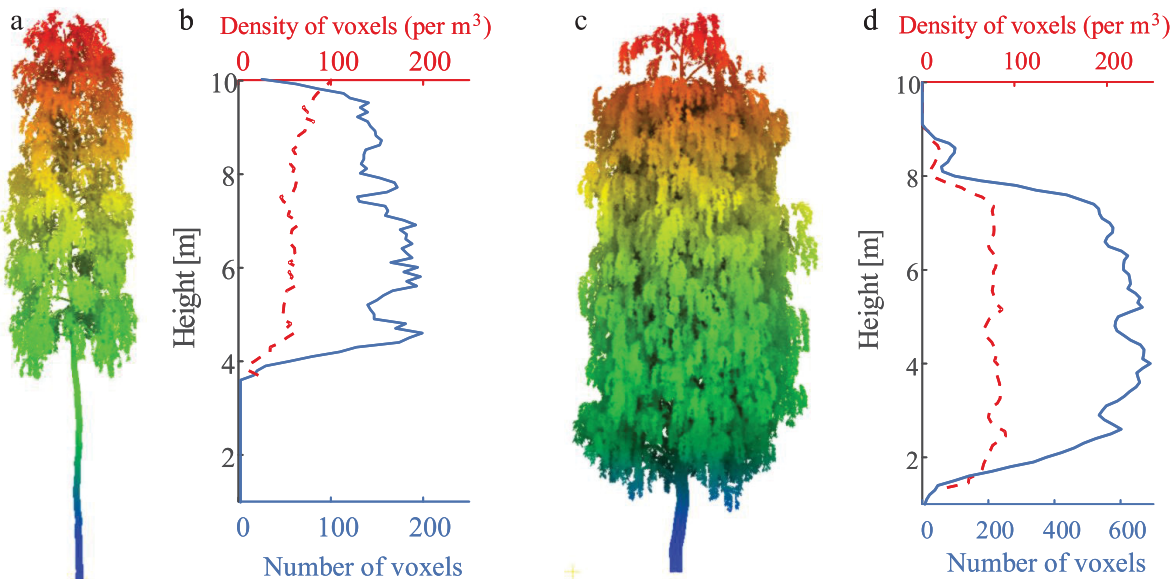


Fig. 5. Tree models used to generate virtual forest scenarios. (a) Tree model for the field forest plots and (c) tree model for the synthetic forest plots and (b) and (d) their vertical profiles.

for airborne and terrestrial LiDAR observations [28]. The HELIOS uses a ray casting method to accurately simulate the 3-D point clouds without simplifying the multiple scattering mechanisms. It considers most of the actual technical specifications, such as beam divergence, pulse energy, sensor area, Gaussian temporal and spatial shapes of the pulse, optical properties of every element in the scene, and multiple scattering. The reflectance of every element is assumed to

be Lambertian. Extensible mark-up language (XML) files are used to define the scanner, platform, and scene models and to configure the behavior of the modules. A graphical interface of interactive real-time 3-D visualization of the simulated surveys is provided in the HELIOS.

For the configuration of the laser scanner in this study, the parameters of the Riegl VZ-400 model were adapted (Table II). The scanner was installed at 1.5 m above ground

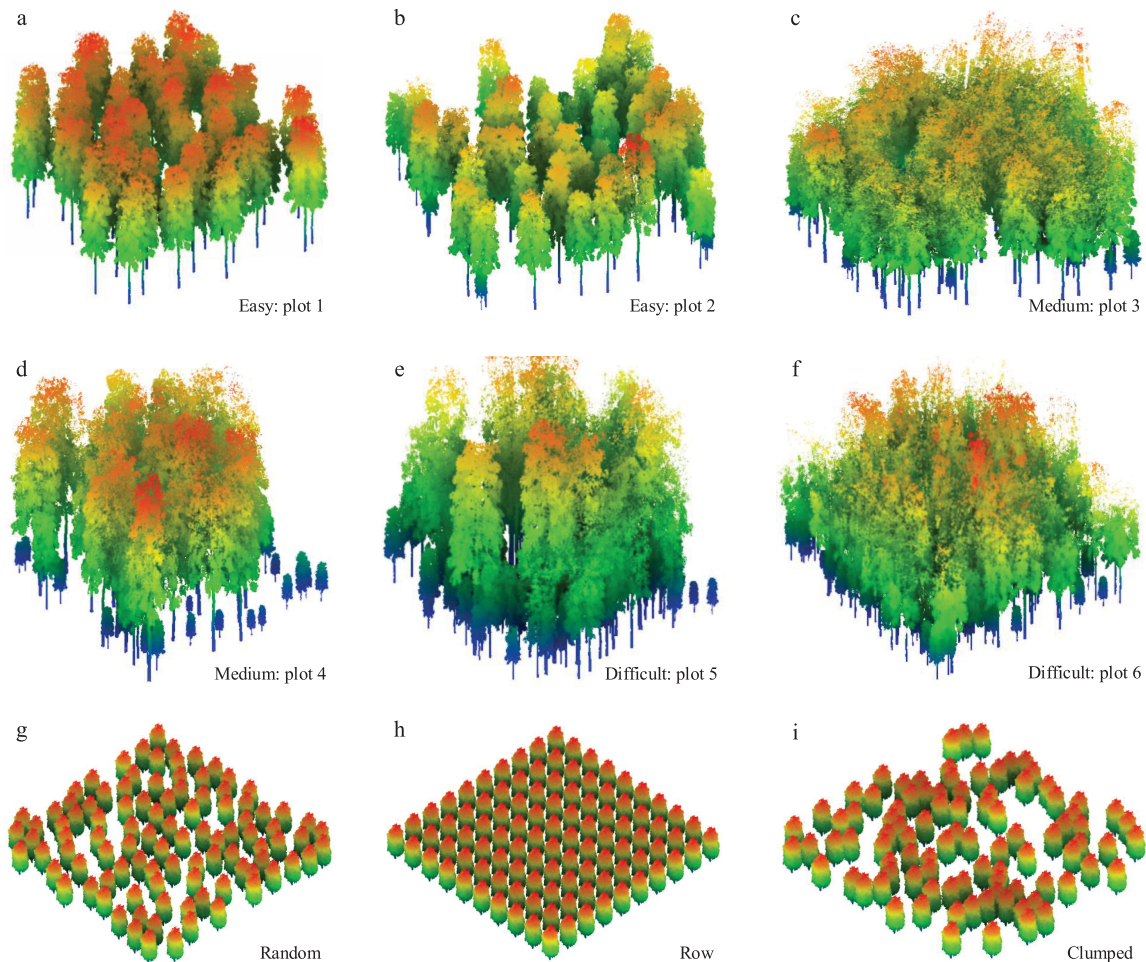


Fig. 6. Visualization of the forest plots used in this study. (a)–(f) Simulated TLS point clouds of the field forest plots (“easy,” “medium,” and “difficult”). (g)–(i) Three examples of the simulated TLS point clouds of the synthetic forest plots (random, row, and clumped distributions).

TABLE II
CONFIGURATION OF THE TLS SIMULATION BY
THE HELIOS IN THIS STUDY

Property	Configuration
Laser scanner	Riegl VZ-400
Scanner height	1.5 m
Field of view	$360^\circ \times 310^\circ$
Angle increment	0.036°
Scan line frequency	24 Hz
Pulse frequency	10000 Hz
Beam divergence	0.35 mrad
Accuracy	0.5 cm

level. The beam divergence was fixed at 0.35 mrad. The scan line frequency and pulse frequency were adjusted to assure that both the horizontal and vertical angular increments were 0.036° with a field of view of $360^\circ \times 310^\circ$, which were

consistent with those in the benchmarking project [27]. In each plot, hemispherical TLS measurements were simulated on the basis of the iterative- and regular-mode scan designs.

C. Preprocessing of the Simulated TLS Point Clouds

The preprocessing of the simulated TLS point clouds includes coregistration of multiple scans, extraction of individual trees, and voxelization of point clouds. Note that the voxelization step was applied only for the point clouds of the synthetic plots because the voxels were used to analyze the occlusion effect of the tree crown.

After the TLS simulation for a scan design, all the simulated hemispherical laser measurements were coregistered into a comprehensive data set of 3-D point clouds for one plot. The hemispherical scans of a plot have an identical coordinate system defined by the HELIOS; thus, the coregistration process does not induce any error.

The point cloud of each individual tree was extracted from the comprehensive point clouds according to the property value of the OBJ_ID field in the output text file of the HELIOS simulation. The OBJ_ID is the identity of the respective object in the scene, starting with “0” and corresponding to the order of objects as stored in the scene XML file. No error exists

during the extraction process for all the field and synthetic plots. The extracted point clouds were used to analyze the completeness of the TLS scan sampling and to estimate the tree attributes, i.e., DBH, tree height, stem curve, and crown volume.

Although point clouds can precisely describe the 3-D structure of trees, they cannot be directly used to assess the occlusion effect because points have no area or volume. Comparably, the voxelized point cloud is a suitable data format for analyzing the vertical distribution of the occlusion effect. A voxel is defined as a cubic volume that can more homogeneously characterize the crown structure than the point cloud. The reference and simulated point clouds of each tree crown were voxelized into 3-D voxel arrays. The voxel size was set to be $10\text{ cm} \times 10\text{ cm} \times 10\text{ cm}$ to ensure a sufficiently detailed level. This voxel size is reasonable because the footprint of the laser beam is less than 10 cm within the $50\text{ m} \times 50\text{ m}$ plot. This setting is also in line with the recommendations of previous studies [16], [29]. All the voxels were identical in volume and shape but different in the number of points that they contained. To evaluate the vertical distribution of the occlusion effect, crown voxels were classified into two classes with the “filled” and “other” attributes based on the beam–voxel interaction [6]. The “filled” attribute was assigned to the voxels that had at least one point intercepted with a laser beam (nonoccluded). The “other” attribute was assigned to the voxels, wherein the laser beams were obstructed before passing these voxels (not reached by any laser beam, i.e., occluded) and the voxels without any interaction with beams (the laser beam passed). This classification was conducted for both the reference and simulated TLS point clouds.

D. Methods for Tree Attribute Estimation

This section details the algorithms for estimating the tree attributes from the simulated point clouds and deriving the reference information from the reference point clouds. As shown in Table I, the DBH, tree height, and stem curve were extracted for the field plots, while the crown volume was estimated for the synthetic plots.

1) *DBH and Tree Height*: In the DBH calculation, we first extracted a horizontal slice from 1.25 to 1.35 m above the calculated tree position. The z -axis information of this slice was removed; thus, the slice was squeezed into a 2-D point cloud. The DBH was then computed by a least-squares regression method with an algebraic estimation of the circle and a geometric reduction of the squared distances to the computed circle [30]. The tree height was obtained through the difference in the z coordinates between the highest point of the tree point cloud and the tree base position.

2) *Stem Curve*: The premise of stem curve estimation is the extraction of a stem point cloud from an individual tree point cloud. The simulated stem points of each tree were identified based on the known tree positions and the convex hull of the corresponding reference stem points. The obtained points were dominated by the stem component and mixed by a small portion of branches and foliage points of neighboring stems. The stems within the tree crowns were

partially missing or blurred because of the occlusion effect. The severity of this problem varied from plot to plot and from tree to tree, depending on the stand situations (stem density and foliage area density) in the plots.

In the stem curve calculation, an open-source forest TLS data processing tool called 3DForest was applied [31]. It can derive the central coordinates and diameters of the fitted circles at different height layers, starting from the lowest height of the stem points followed by a specific height increment (i.e., 20 cm in this study) using a Randomized Hough Transform algorithm [31]. If the number of points found at a particular height layer is less than three, the diameter at this height cannot be estimated and was assigned to null in the 3DForest. To evaluate the completeness of the stem points and the stem curve estimation accuracy for individual stems, we introduced a stem completeness index (SC), which is defined as the ratio of the number of measured diameters to the number of height layers for a stem [15]. This index was calculated separately for the part of the stem in the crown (SCB) and the part of the stem below the crown (SCI), for all the plots.

3) *Crown Volume*: The crown volume of an individual tree was calculated using the alpha shape algorithm with an alpha radius of 0.3 m after removing the stem points below the crown base height [7]. The alpha shape function provides a concave hull to capture the exact crown shape. This cube size was selected according to the point density. The reference crown volume was 44.466 m^3 in synthetic plots.

IV. RESULTS

A. Visualization of the PoTo Index Maps and Optimal TLS Location

The PoTo index maps of three field plots in the first and second iterations are shown in Fig. 7. The spatial pattern of the PoTo index varies with the iterations because the input trees are different for each iteration (see Section II-A4 and Fig. 1). For the first iteration [Fig. 7(a), (c), and (e)], the areas with a relatively high PoTo index (yellow areas) are usually located in the central and sparse regions. In contrast, the lower values are mainly distributed at the border and corner regions. Consequently, the first TLS location tilts to the central and sparse area of the plot, which is also reflected in the regular-mode design. For the second iteration [Fig. 7(b), (d), and (f)], the distribution of high values is spatially dispersed, and high values can appear in any region. At the same time, the location of the first TLS location and its adjacent area characterize low values, which indicates that different TLS locations would not be overly concentrated. With the integral action of the PoTo index map and CDRC statistic, the second TLS location was selected at the position away from the first location, which usually presented at the border and corner regions, and it provided optimally complementary sampling to the first TLS scan. The spatial pattern of the PoTo index also depends on the stem density, tree size, and tree distribution. A higher stem density leads to more severe occlusion effect. Note that the range of the colormap is different for different plots. Therefore, quantification of the occlusion effect can provide an indicator for exploring the optimal TLS locations.

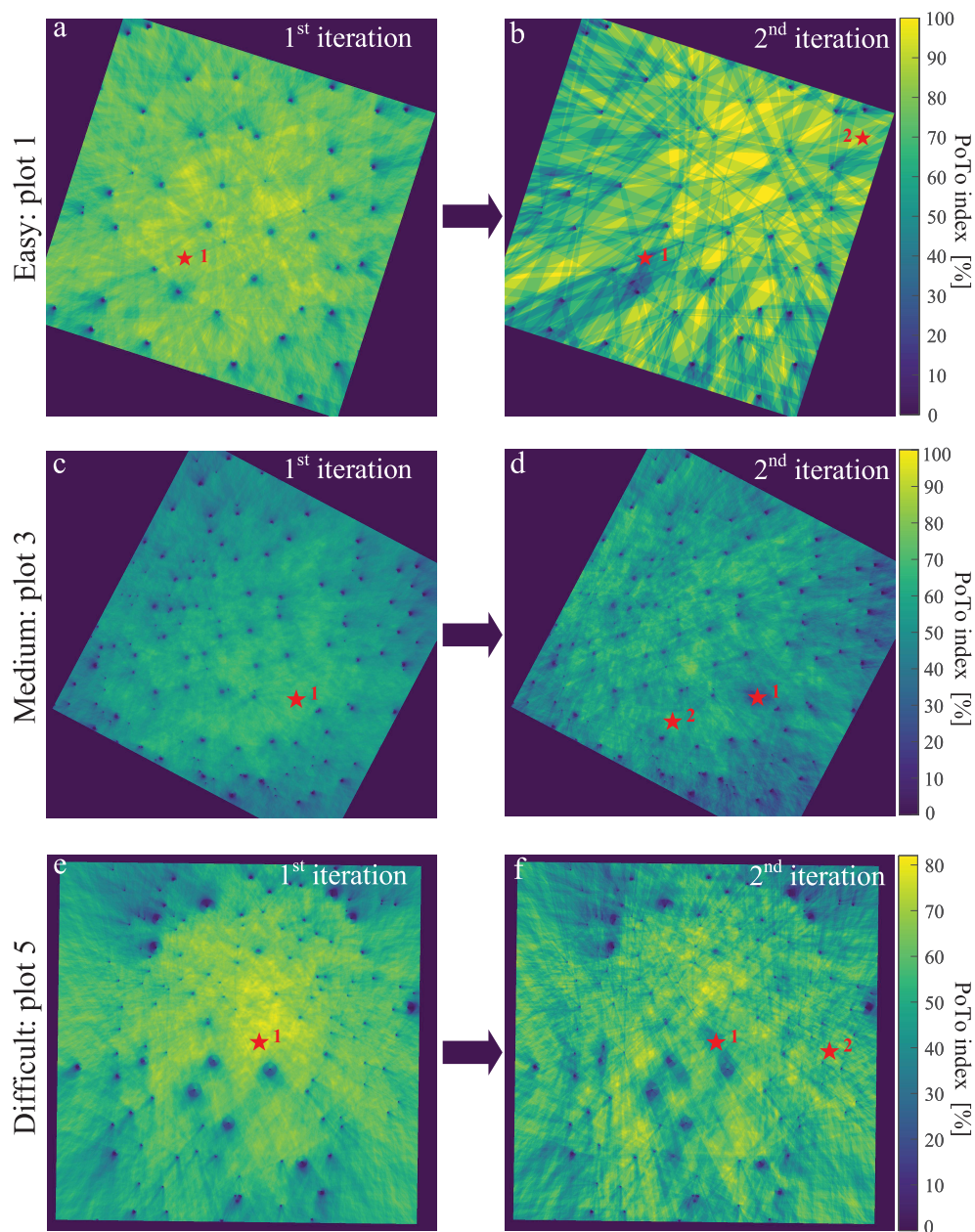


Fig. 7. Maps of the PoTo index for three field plots and visualization of determining the optimal TLS locations (red stars) in the first and second iterations: (a), (b) plot 1, (c), (d) plot 3, and (e), (f) plot 5.

B. Comparison of the Scan Completeness Between Two Scan Designs

Fig. 8 shows the variation in the detection rate with the cumulation of scans for six field plots. In the iterative-mode design, there are four scans for “easy plots” and five scans for “medium” and “difficult” plots. In the regular-mode design, every plot was scanned by five TLS scans. It should be noted that the meanings of the detection rate for the first scan and other scans are different. The operator-expected CDRC (T_E) of the first scan and the other scans was set to 120° and 200° , respectively (see Section II-A4). This difference might explain why the cumulation of more than one scan sometimes provided a detection rate lower than that provided by the first scan. In “easy” plots, the iterative-mode design enabled a better detection rate fewer less scans than the regular-mode

design. In “medium” and “difficult” plots, the iterative-mode design always performed much better on the detection rate. The detection rate of all the scans of a plot is expected to be as close to one as possible in the iterative-mode design, which intuitively demonstrates that the iterative-mode design was more suitable for handling the plots that had a higher stem density (plot 3, plot 5, and plot 6).

To assess the scan completeness for the iterative- and regular-mode scans, we compared the probability histogram of the CDRC of the tree circles. As illustrated in Fig. 9, the CDRCs of the trees were classified into three categories: 0° – 120° , 120° – 200° , and 200° – 360° , which were labeled as “insufficient,” “intermediate,” and “fine.” Overall, the iterative-mode design achieved higher probability for the “fine” class, especially for the cases with higher stem density

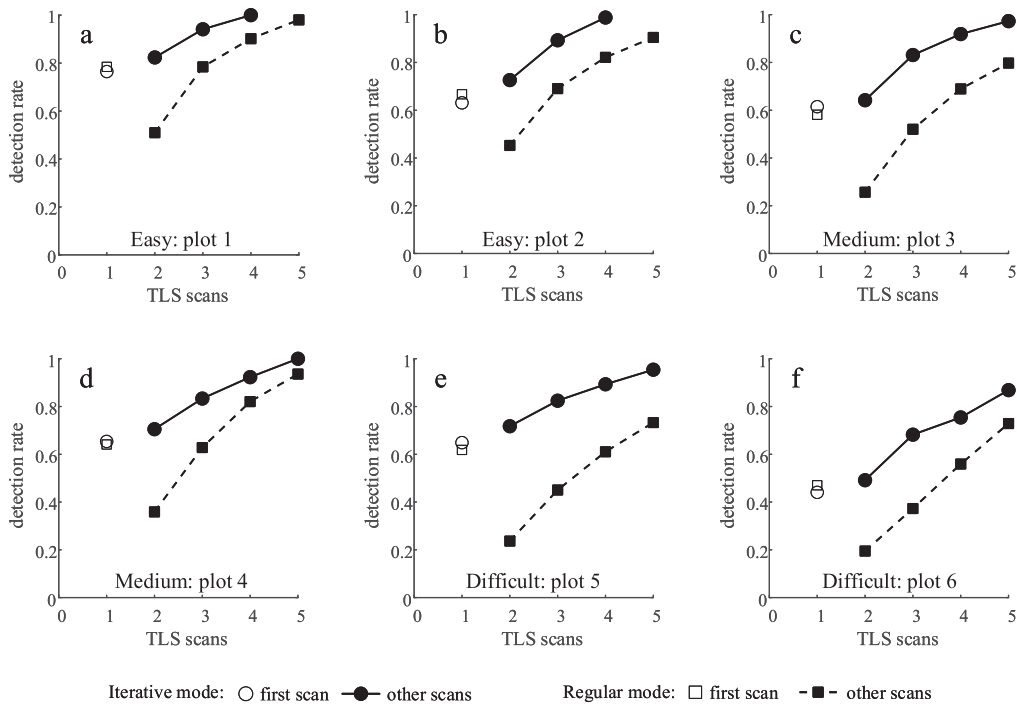


Fig. 8. Variation in the detection rate with the cumulation of scans for six field plots (a)–(f). In the calculation of the detection rate, the operator-expected CDRC of the first scan and the other scans were set to 120° and 200° , respectively.

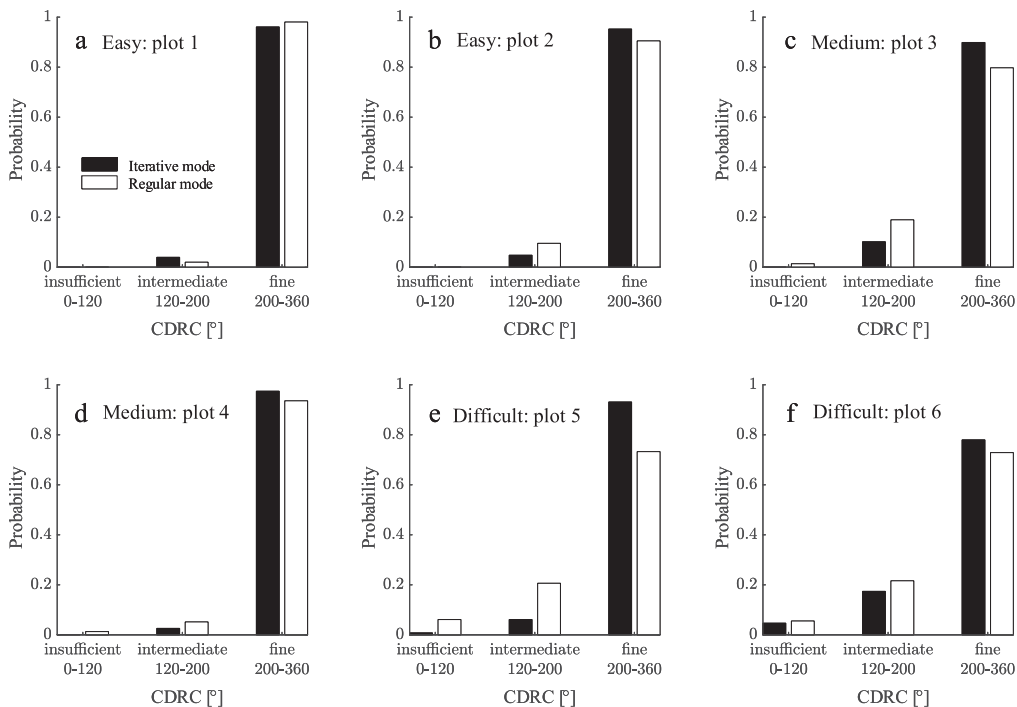


Fig. 9. Comparison of the CDRC of the trees between the iterative- and regular-mode scan designs in six field plots (a)–(f).

(plot 3 and plot 5). In addition, the iterative-mode design resulted in a lower probability for the “insufficient” class, approaching zero for the “medium” plots and even for the “difficult” plots, which implies that almost no trees were sampled with a CDRC of less than 120° in the iterative-mode design. These findings revealed that the new proposed design

can achieve more complete scanned data and, thus, improve the quality of the scans. In contrast, the regular-mode design yielded a larger probability in the case of the “intermediate” class. Fig. 9 also suggests that the iterative-mode design has more potential to mitigate the occlusion effect under high-stem-density conditions (i.e., “medium” and “difficult” plots).

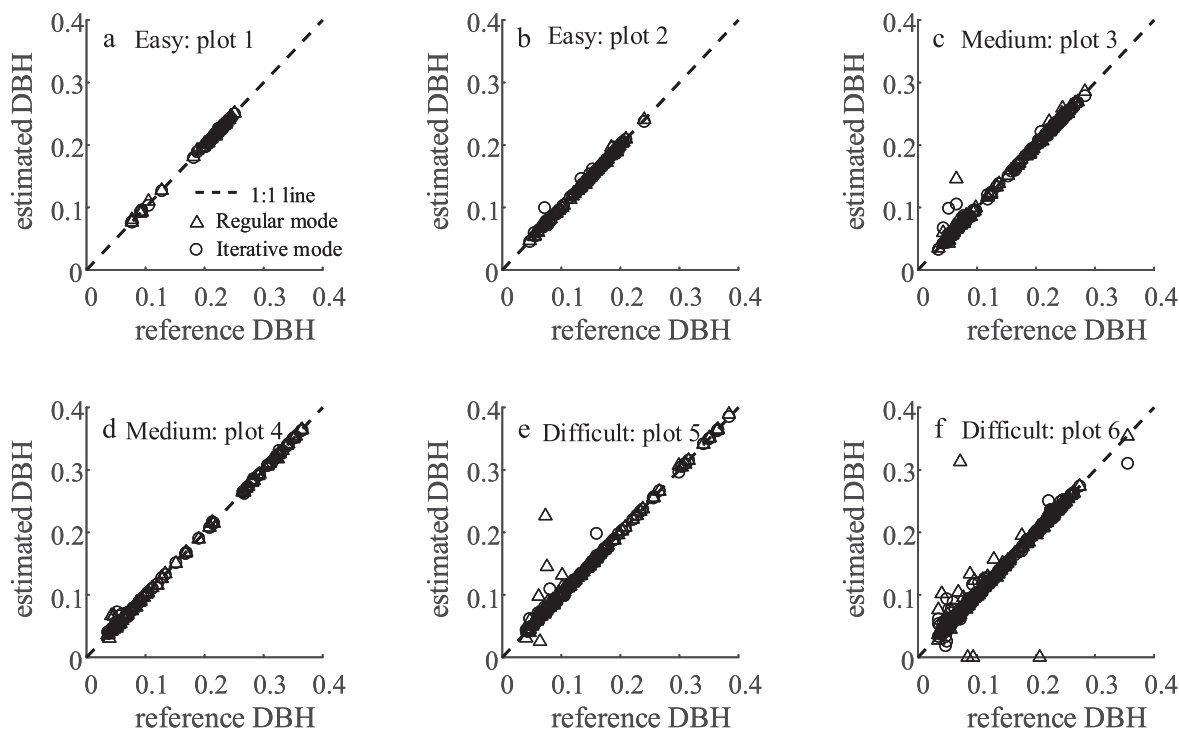


Fig. 10. Comparison of the DBH derived from scans between the iterative- and regular-mode designs in the field plots (a)–(f). The unit of the DBH is meter.

TABLE III
RMSES OF STEM ATTRIBUTE ESTIMATES DERIVED FROM ITERATIVE- AND REGULAR-MODE SCANS FOR ALL FIELD PLOTS

Metric	Scan design	DBH (cm)			Tree height (cm)		
		“easy”	“medium”	“difficult”	“easy”	“medium”	“difficult”
RMSE	Iterative	0.28	0.51	0.62	6.78	20.47	23.53
	Regular	0.16	0.64	1.78	7.60	21.67	46.36

C. Comparison of Stem Attribute Estimates

The comparisons of the DBH estimates derived from the iterative- and regular-mode point clouds are presented in Fig. 10. The estimation accuracy of DBH decreased with the increase in the complexity (“easy,” “medium,” and “difficult”) because the completeness of the TLS data decreases with complexity, as shown in Table III. The estimated DBH values from both designs are well correlated with the reference values for the “easy” plots. However, the iterative-mode estimates have better agreement with the reference values for the “medium” and “difficult” plots (the mean root-mean-square error (RMSE) of DBH is 0.57 cm), whereas the regular-mode design was shown to obviously overestimate the DBH of several stems (the mean RMSE of DBH is 1.21 cm). In particular, the regular-mode design produced three severely underestimated DBH in plot 6 (DBH = 0) due to the full obstruction for the 1.3-m-height layer of these stems. Accurate DBH estimation requires a transect that includes points as much as possible and stems with a CDRC of larger than 200°, and thus, for the stems from the “insufficient” and

“intermediate” class (see Fig. 9), it is usually difficult to obtain sufficient intensity transect information for a reliable diameter estimation.

Fig. 11 shows a comparison of the tree height estimates between the two scan designs. The results show good correlation with the reference values for both designs (e.g., RMSE = 20.47 cm for the iterative mode and RMSE = 21.67 cm for the regular mode in the “medium” plots, see Table III). Only a small portion of trees was underestimated with the regular-mode design for the most “difficult” plot (plot 6) with the highest tree density, due to the intense occlusion effect of the canopy elements.

The accuracy of the stem curve estimation from the two scan designs was interpreted from Fig. 12. Additionally, to measure the effectiveness of the stem diameter estimation at the part within the crown and the part below crown, two evaluation factors, i.e., SCI and SCB defined in Section III-D2, were investigated. Technically, the SCB values were always higher than the SCI values due to the severe obstruction problem within the crown [32]. The stem curve estimation

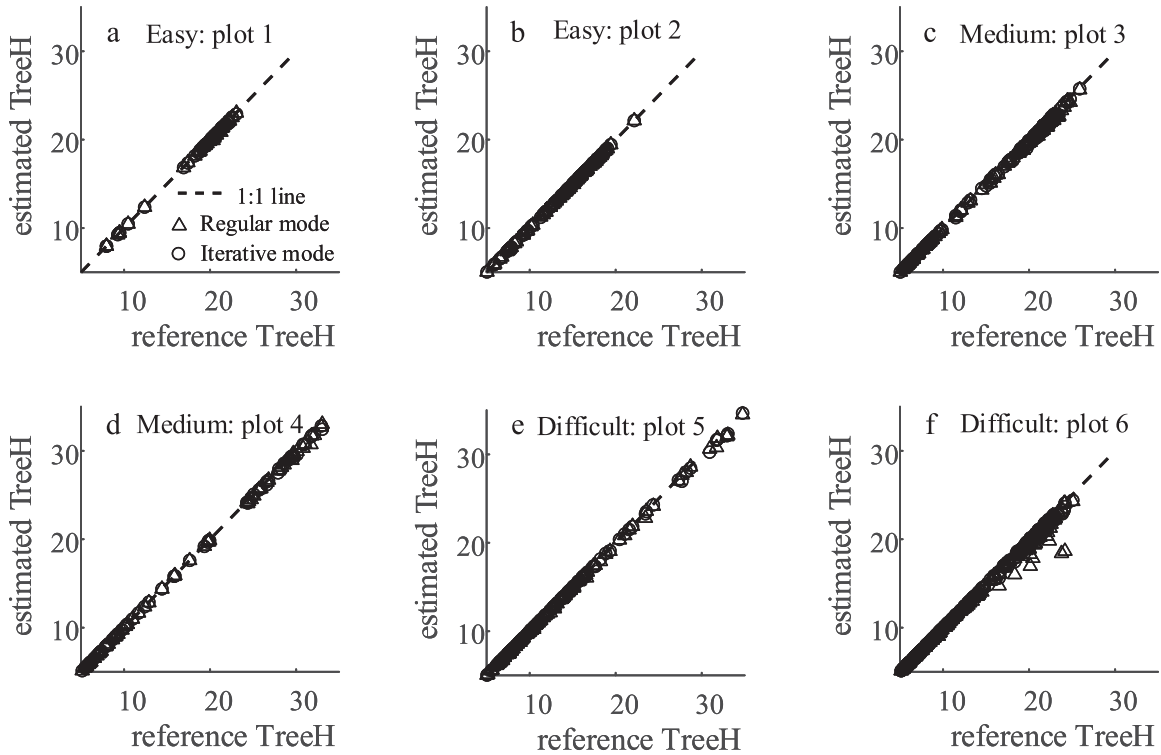


Fig. 11. Comparison of the tree height derived from scans between the iterative- and regular-mode designs in the field plots (a)–(f). TreeH refers to the tree height with the unit of meter.

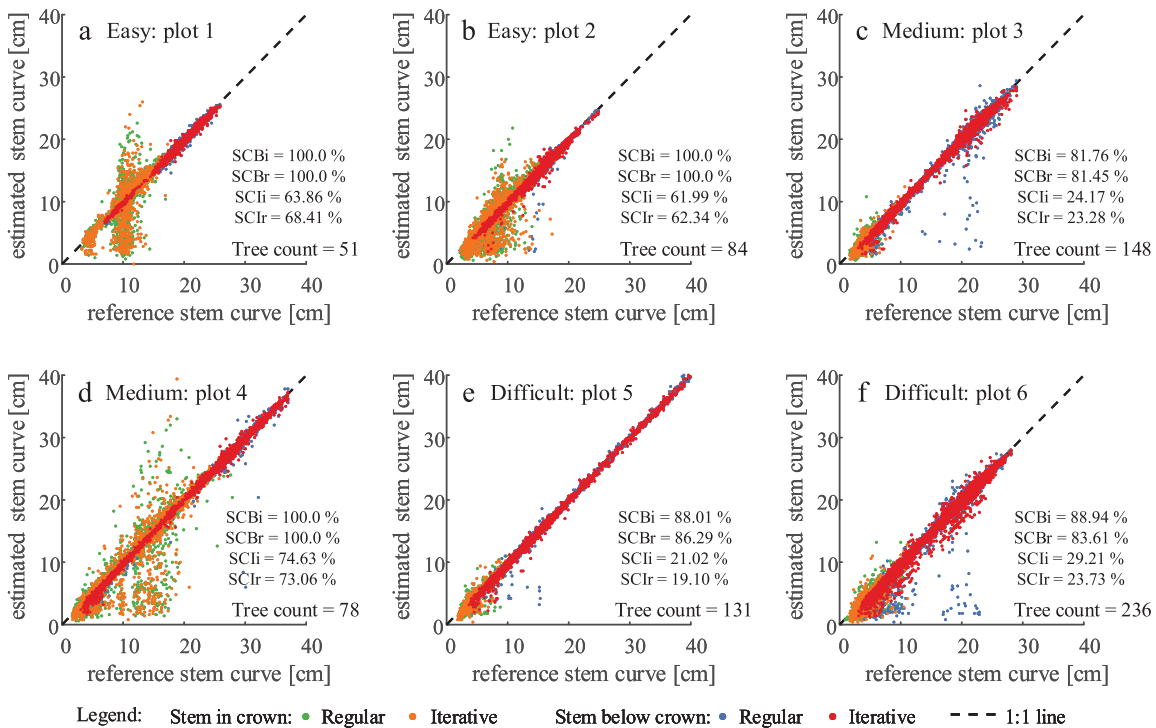


Fig. 12. Comparison of stem curves derived from scans between the iterative- and regular-mode designs in the field plots (a)–(f). The stem diameter estimates were calculated for the part within the crown and the part below the crown (see Section III-D2). The subscripts *i* and *r* of SCI and SCB refer to the iterative- and regular-mode designs, respectively.

for the stem within the crown (Fig. 12). Unexpectedly, similar estimation accuracies of the stem curves between the stems

below the crown and within the crown were observed for high-density plots (plots 3, 5, and 6). This phenomenon can be explained by the lower SCI, which implies that the stems

TABLE IV
RMSES OF THE STEM DIAMETER ESTIMATES DERIVED FROM ITERATIVE- AND REGULAR-MODE SCANS FOR ALL THE FIELD PLOTS

Metric	Scan design	Stem curve (below crown, cm)		
		“easy”	“medium”	“difficult”
RMSE	Iterative	0.48	0.72	1.01
	Regular	0.58	1.08	1.65

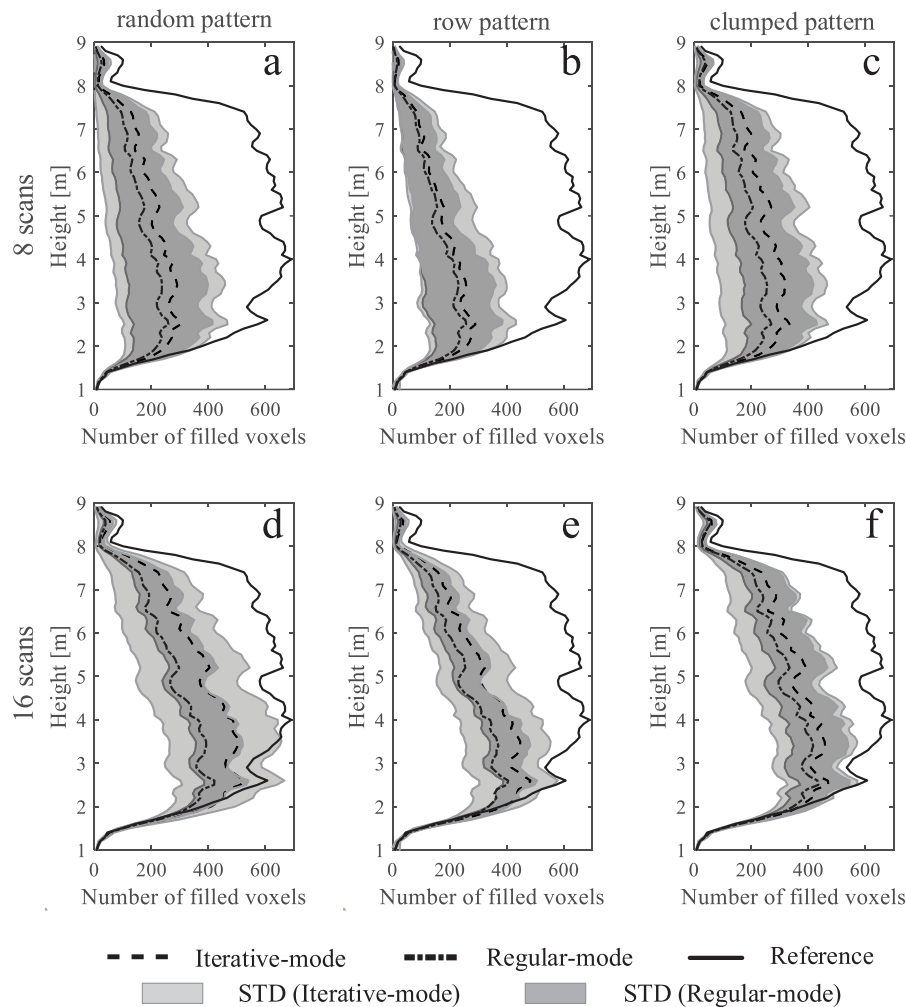


Fig. 13. Comparison of the vertical profiles of filled voxels derived from iterative- and regular-mode scans in synthetic lots [(a)–(c) are with eight scans and (d)–(f) are with 16 scans]. STD is the abbreviation of the standard deviation.

within the crown were rarely detected. For example, SCiI was 61.99% for plot 2 but 21.02% for plot 5. In the stem diameter estimation with the crown, the stem edge points were difficult to locate when the stem was partly obscured by the canopy elements, which causes difficulty associated with circle fitting. In contrast, the extracted stem diameters at different height slices of the stem below the crown were comparable with the reference measurements. The scatter points that belong to the iterative-mode design were more concentrated along the 1:1 line, compared with the regular-mode design. The new

proposed design enabled the robust and accurate estimation of the stem curve at various tree ages and different stem densities (RMSE < 1.1 cm, see Table IV), where a sparser forest led to better results (e.g., lower RMSE for “easy” plots against “difficult” plots). Comparably, it was pronounced that many substantially misestimated stem diameters (± 20 cm) were observed for the regular-mode design [see the blue dots with large bias in Fig. 12(c), (e), and (f)], especially in the plots with high stem density (the RMSE is up to 1.65 cm).

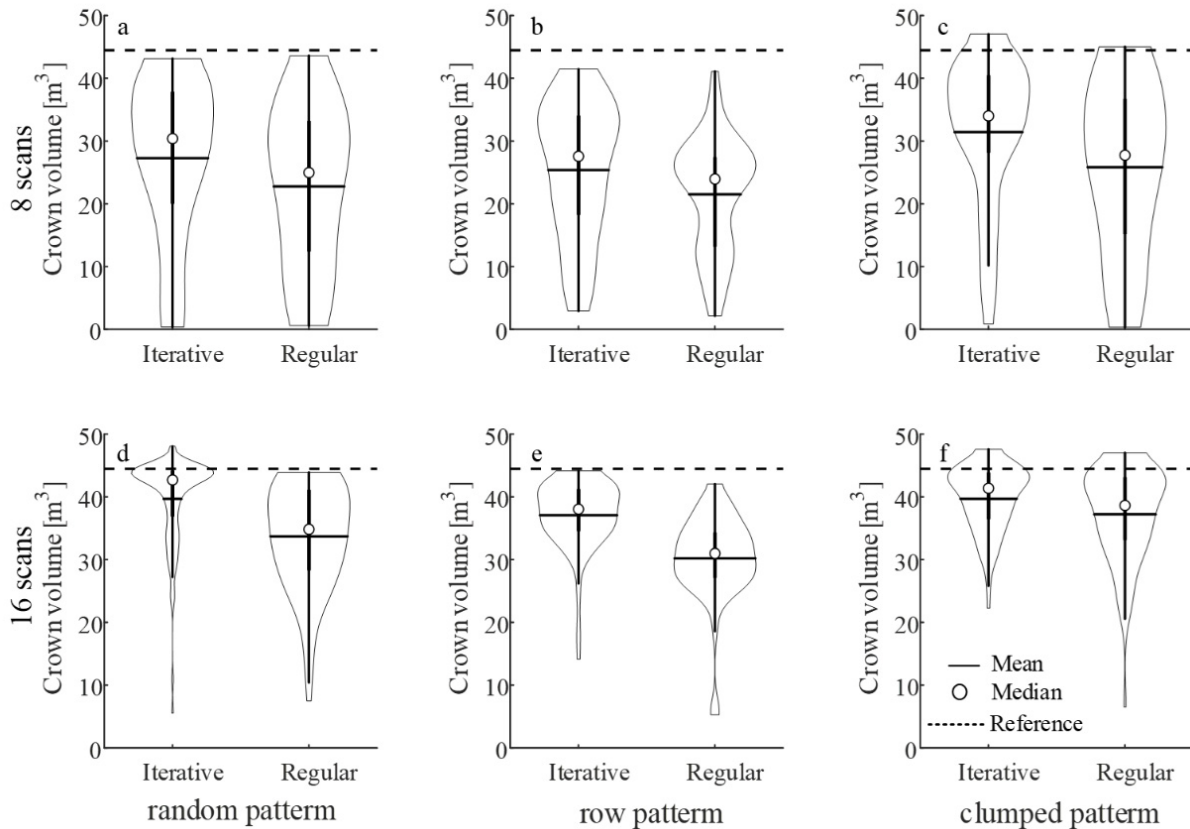


Fig. 14. Comparison of the crown volume derived from the TLS point cloud between the iterative- and regular-mode designs in the synthetic plots [(a)–(c) are with eight scans and (d)–(f) are with 16 scans].

D. Comparison of Crown Attribute Estimates

Fig. 13 illustrates the comparison of the vertical profiles of the filled voxels derived from the simulated point cloud of the tree crown for the iterative- and regular-mode designs. The occlusion effect caused by the leaves is prominent for the two designs, and the measured profiles show large underestimation compared to the reference profile, especially in the upper layers of the crown. However, this underestimation is larger in the regular-mode scans than in the iterative-mode scans. The reason is that the tree model of this study has dense foliage and branches at the crown outskirts, which causes the laser beams to hardly pass the crown outskirts and interact with the interior elements, and thereby, there is a large proportion of TLS points that are located at a low height level.

Fig. 14 shows a comparison of the crown volume estimates between the iterative- and regular-mode designs with 8 [Fig. 14(a)–(c)] and 16 [Fig. 14(d)–(f)] scans. The violin plots highlight the difference between the crown volume estimated from the two modes through probability densities. For the regular and iterative modes, the estimates usually underestimated the reference crown volume regardless of the tree pattern and number of scans. The results show that the estimates derived from the iterative-mode design are less erroneous (lower RMSE) than those derived from the regular-mode design (Table V). For example, the RMSE of the crown volume estimates is 9.155 m^3 for the iterative-mode design but 15.822 m^3 for the regular-mode design in the

row plot [Fig. 14(e)]. A larger proportion of estimates is close to the reference value for the iterative-mode design, compared with the regular-mode design. Most of the estimates are consistent with the reference value in the 16-scan comparison, which indicates that the additional scans effectively improve the accuracy of the crown volume estimation. Table V shows the RMSE of the crown volume for each type of pattern. The iterative-mode design made a large improvement in the accuracy of the crown volume estimation, especially for random- and row-pattern plots (Table V) with 16 scans. The ratio of the RMSE to the reference decreased by up to 15% via the iterative-mode design in the row-pattern plots.

V. DISCUSSION

A. Feasibility of the 2-D Simplification of Trees

The optimization of the iterative-mode scan design is based on the 2-D simplification of the tree, i.e., a 3-D tree is represented by a circle. Evidently, the 3-D quantification of occlusion over forest ecosystems is a highly complex and time-consuming task [29]; hence, investigating the scan design with a 3-D realistic structure is impractical. Quantifying the occlusion effect in 2-D space is more straightforward and less time consuming than that for a 3-D shape [24], [25], [33], [34]. The 2-D simplification facilitates an appropriate and flexible computation of visibility analysis and the determination of TLS locations by using the CDRC. In the input information, the tree location is considered according to the center of the

TABLE V
RMSES OF THE CROWN VOLUME ESTIMATES DERIVED FROM ITERATIVE- AND REGULAR-MODE SCANS FOR THE SYNTHETIC PLOTS. THE 8- AND 16-SCAN DESIGNS WERE ASSESSED. THE PERCENTAGE REFERS TO THE RATIO OF THE RMSE TO THE REFERENCE VALUE

Scans	Scan design	Crown volume (m ³)		
		Random	Row	Clumped
8 scans	Iterative-mode	21.216 (17.8%)	21.933 (49.2%)	17.331 (38.8%)
	Regular-mode	25.157 (56.6%)	24.630 (55.4%)	22.927 (51.6%)
16 scans	Iterative-mode	8.621 (19.4%)	9.155 (20.6%)	7.037 (15.8%)
	Regular-mode	13.514 (30.8%)	15.822 (35.7%)	10.221 (23.1%)

circle, and the tree size is characterized by the circle diameter. We suggest that the tree size can be the DBH or crown diameter depending on different applications. For example, 3-D forest modeling, which is usually one of the main purposes of a TLS campaign, usually focuses on all the tree elements, including the stem, branches, and leaves, thereby needing the crown diameter as the tree size to produce a full plot coverage [4]. Different tree sizes theoretically lead to different optimal scan locations because the corresponding visibility maps (or PoTo index maps) would significantly change even under identical tree locations. A large tree size induces a strong occlusion effect for a given tree pattern and changes the spatial distribution of the occlusion effect, which results in limited areas to place the scanner. Such an increase in the occlusion effect illustrates the importance and difficulty of placing the scans when attempting to retrieve the crown variables or even the DBH in dense forest plots. In this context, the iterative mode design can be especially helpful for operators in determining the optimal scan locations. In practice, the tree sizes input to the iterative scan design are recommended to be modestly larger than the actual values, to minimize the uncertainty caused by the inaccurate tree size measurements.

B. Influences of the Occlusion Effect on the TLS Location, Scan Completeness, and Tree Attribute Estimation

The PoTo index maps of various plots highlighted that the occlusion effect is highly related to the spatial pattern, tree density, and tree sizes (Fig. 7). Quantification of the occlusion effect offered an insightful way to optimize the TLS locations. From the perspective of developing a good scan design, the sampling of multiple scans should have low redundancy and should be complementary to one another. Both the iterative- and regular-mode designs attempted to achieve this goal, wherein the former design has the potential to minimize the redundancy and maximize the complementary sampling. The iterative-mode scan locations are usually distributed in sparse regions, which differ from the fixed center and corner regions in the regular-mode design.

The scan design without considering the exact occlusion effect might lead to unfavorable sampling (Figs. 8 and 9).

The improvement in the detection rate by using the iterative-mode design demonstrates that the optimization of the TLS locations based on the quantification of the occlusion effect is effective, especially for more complex environments, e.g., “medium” and “difficult” plots (Fig. 8). The statistical results of the CDRC of tree circle explicitly illustrate the differences in the sampling completeness between the two designs in ideal situations (Fig. 9). The results shown in Fig. 9 also validate that the new proposed algorithm can maximize the complementary sampling among multiple scans. More trees with “fine” CDRC and less trees with “insufficient” and “intermediate” CDRC would theoretically improve the accuracy of the tree attribute estimation (Figs. 10–14), thereby indicating the merit of the new design. However, extremely high-density stems would buffer the merit (e.g., plot 6).

In stem attribute estimation, both the regular- and iterative-mode designs yielded good results, although the former caused low-accuracy estimates of several stems (Figs. 10–12). The estimation accuracy of the tree height is less influenced by the obstruction among the stems because the tree height estimation depends on only the highest and lowest points. Thus, the estimates of the tree heights by the two designs are almost identical except for the most “difficult” plot (plot 6, Fig. 11). The DBH and stem curve estimation are severely affected by the occlusion effect. Consequently, the better estimates by the iterative-mode design are observed in all the “medium” and “difficult” plots. Differing from the regular-mode design, the new design can capture every stem (Figs. 10 and 12). We, therefore, believe that the regular-mode design is appropriate for “easy” plots and some “medium” plots, and the iterative-mode design should be recommended for “medium” and “difficult” plots if the surveyors require accurate recognition for each stem.

For the occlusion effect along the vertical direction (Fig. 13), both scan designs show an evident negative bias with a reference profile, especially for the upper layers of the crown. This result implies that neither the iterative mode nor the regular mode can achieve a good sample inside the crown due to the obstruction of the highly dense foliage at the crown outskirts. Additional scans from different directions, increasing the possibility of interaction with interior elements,

TABLE VI
RMSEs OF THE STEM ATTRIBUTE ESTIMATES DERIVED FROM THE BIASED ITERATIVE-MODE SCANS WITH RANDOM ERRORS FOR ALL THE FIELD PLOTS

Metric	Attribute	Category		
		“easy”	“medium”	“difficult”
	DBH (cm)	0.31	0.55	0.72
RMSE	Tree height (cm)	6.75	19.87	25.69
	Stem curve (cm)	0.51	0.77	1.26

can effectively reduce the occlusion effect and improve the data quality. In addition, the negative bias is also determined by the tree distribution. As the crown base height is almost 1 m and the scanner height is 1.5 m, the number of filled voxels can approach the reference value at approximately 2 m (Fig. 13). As expected, the occlusion effect usually increased with the height because the laser beam could not reach most of the treetops and the point density in the upper crown was rather low. This problem might be reduced by using a high-height multipulse mode LiDAR. In the estimation of crown attributes, the iterative-mode design obtained more complete sampling and yielded more accurate results than the regular-mode design. An important fact is that the iterative-mode design showed considerably different performances among the three types of tree patterns (Fig. 14). The crown attribute estimates are closer to the reference value for the random and row patterns than for the clumped pattern. Thus, clumped trees would reduce the sampling capability of the TLS. Nonetheless, the iterative-mode design greatly improved the scan completeness and the accuracy of the crown attribute estimates for the nonclumped scenarios.

C. Influence of Inaccurate Recognition of the Scan Location in the Field

The recognition of scan locations is a challenging work in the field due to the possibility of inaccurate positioning. The manner of conveniently recognizing the positions of predetermined iterative-mode scans in the field is a key problem due to the unstable performance typical of a GPS in forest areas [35]. A possible solution is to use differential GPS to improve the GPS measurement accuracy or to use a Haglöf PosTex ultrasound instrument (Långsele, Sweden) for the positioning of objects in the forest plots. Unmanned aerial vehicles (UAVs) with high-accuracy real-time kinematic units would guide the TLS placement. If repeat campaigns (e.g., leaf-on and leaf-off) are planned, then marking the location of each scan position (e.g., with a small flag or stake) is beneficial. However, even with the assistance of these instruments, inaccurate recognition remains; thus, this problem could lead to modified scan completeness. Moreover, highly complex forest environments have obstacles to the practical placement of laser scanners and their accessories.

Given the above, it is crucial to launch a quantitative sensitivity analysis of the scan location. A random error that

ranges from 0.5 to 2.5 m [36] at random azimuth directions was added onto each iterative-mode TLS location of every field plot. The corresponding point clouds under the biased TLS scans were simulated by the HELIOS. We derived the stem attributes from these point clouds according to the methods described in Section III-D and then compared them with the results illustrated in Section IV-C. According to the joint interpretation of Tables III, IV, and VI, the overall estimation accuracy of the stem attribute is slightly decreased due to the biased scans (e.g., the RMSE varied within 0.3 cm for the stem curve). Notwithstanding, the biased iterative-mode scans still enabled high-accuracy estimation in terms of the DBH, tree height, and stem curve, which verifies the performance of the new proposed design, especially for high-density plots.

D. Limitations of the Iterative-Mode Design and Possible Solutions

Although the iterative-mode scan design proved its advantages in alleviating the occlusion effects in our simulation, several factors might limit the usage of this design in the field. The first is the identification of individual trees. Overall, remote sensing methods are available for detecting individual trees and generating tree location maps, e.g., using UAV-based LiDAR/structure-from-motion (SfM) point clouds [22], [23], thereby efficiently enabling the database to determine the iterative-mode scans. However, the currently reported methods that are used to identify individual trees are suboptimal, especially for highly complex forests with competition among trees [37], [38]. Missing trees would lead to unfavorable iterative-mode scans for the plot. An existing accurate tree location map with a known tree size can be the base data to design iterative-mode scans since such a map is available in many fixed experiment sites. The second factor is the understory vegetation [39], which also causes an occlusion effect in the field measurement in addition to the overstory elements [3]. Because only the spatial pattern and tree size were considered in the determination of optimal scans, the applicability of 2-D simplification must be recognized in various forest understory conditions. For example, in a dense understory vegetation area, a clear view of the tree canopy might not always be possible. A slight shift in the TLS location might reduce this effect, although it might theoretically cause suboptimal scans. Parameterizing the understory vegetation with additional circles might also be a solution. Apart from the above,

the positions of reflectors (i.e., the coregistration targets for multiple scans) might need to be calculated in our future algorithm for facilitating the reflector distribution in the field. Alternatively, an off-the-shelf automatic registration method based on a coarse-to-fine strategy is suggested [20].

Nonetheless, the iterative-mode scan design is expected to be operated and tested in field TLS measurements despite the existing problems, and many applications have shown a demand for further effective scan designs [3], [20], e.g., repeated campaigns aim to improve the data collection efficiency and data quality.

VI. CONCLUSION

A new iterative-mode scan design for minimizing the occlusion effect in TLS measurements was developed in this study. The new scan design used the PoTo index to evaluate the number of trees scanned from a spatial location using an efficient visibility analysis algorithm and to select the effective candidates for the optimal TLS location. The CDRC index was then used to determine the optimal TLS location in each iteration. The iterative-mode design was compared with the regular-mode design, based on the simulated point cloud data sets of virtual field and synthetic forest plots. The results revealed that the proposed design can improve the scan completeness and refine the tree attribute estimation (DBH, tree height, stem curve, and crown volume). Importantly, the iterative-mode design highlighted its merit in medium- and high-density stands, e.g., the RMSE decreased by 38% in the stem curve estimation in “difficult” plots. It is concluded that the regular-mode design is suitable for “easy” plots and some “medium” plots, and the iterative-mode design is valuable for all plot categories, especially for “medium” and “difficult” plots if surveyors prefer higher estimation accuracy of the tree attributes and recognition for each stem. The succeeding efforts should, therefore, be the validation of the iterative-mode scan by using field data set and standardization of field operations.

APPENDIX COMPUTATION OF VISIBILITY ANALYSIS

Our visibility analysis is based on a 2-D simplification of a forest using circles. The visible area can, therefore, be determined by calculating the geometric relationship between the observation point and the objects (i.e., circles). The computation steps are as follows.

- 1) Calculation of the tangent vectors. Given an observation point P and object circle O with a radius r , the tangent points T_1 and T_2 can be determined using the geometric model illustrated in Fig. 15. Points O , P , T_1 , and T_2 are on circle C with radius R . Resolving (A1) provides the solution of the tangent points T_1 and T_2 with the corresponding coordinates. The subscripts x and y refer to the x -axis and y -axis coordinates, respectively. Subsequently, the two tangent vectors (\rightarrow_{PT_1} and \rightarrow_{PT_2})

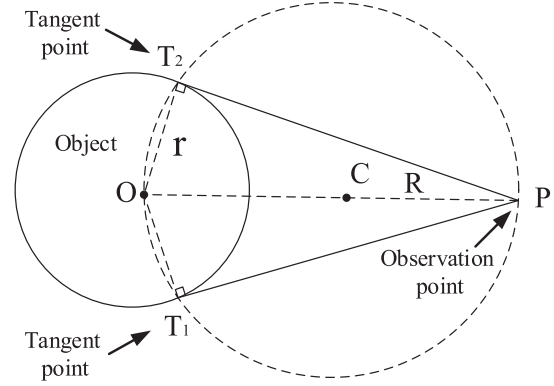


Fig. 15. Illustration of the calculation of the tangent vector between a given point and a circle.

can be derived

$$\begin{cases} (x - O_x)^2 + (y - O_y)^2 = r^2 \\ (x - C_x)^2 + (y - C_y)^2 = R^2 \\ C_x = (O_x + P_x)/2 \\ C_y = (O_y + P_y)/2 \\ R = \frac{1}{2} \sqrt{(P_x - O_x)^2 + (P_y - O_y)^2} \end{cases} \quad (\text{A1})$$

- 2) Recognition of occlusion situations. Given the possible occlusion among the object circles, the occlusion situations must be determined (Fig. 16). The situations of circles (A and B) can be derived with judgment conditions

$$\begin{cases} (\theta_{\max}^A - \theta_{\min}^B) > (\theta_{\max}^A - \theta_{\min}^A) + (\theta_{\max}^B - \theta_{\min}^B), \\ \text{no obstruction} \\ (\theta_{\max}^A - \theta_{\min}^B) \leq (\theta_{\max}^A - \theta_{\min}^A) + (\theta_{\max}^B - \theta_{\min}^B), \\ \text{with obstruction} \end{cases} \quad (\text{A2})$$

$$\begin{cases} \text{sgn}(\theta_{\max}^A - \theta_{\max}^B) = -\text{sgn}(\theta_{\min}^A - \theta_{\min}^B), \\ \text{full obstruction} \\ \text{sgn}(\theta_{\max}^A - \theta_{\max}^B) = \text{sgn}(\theta_{\min}^A - \theta_{\min}^B), \\ \text{partial obstruction} \end{cases} \quad (\text{A3})$$

where a polar coordinate system was created with the center located at the observation point. θ is the angle of the tangent vector, where the subscripts max and min refer to the maximum and minimum polar angles of the tangent vectors, respectively. Here, sgn is the symbol of the sign function. This recognition process was repeated for each tree.

- 3) Calculation of the endpoints of the visible arc. As illustrated in Fig. 16, the endpoints of the visible arc of circle B (taking circle B as an example) have the following situations: 1) two tangent points of circle B during no occlusion [Fig. 16(a)]; 2) a tangent point of circle B and an intersection point between circle B and a tangent line of circle A during partial occlusion [Fig. 16(b)]; and 3) no intersection points during full occlusion [Fig. 16(c)]. In cases 1 and 3, the end intersection points are the tangent points. In case 2, the x - y coordinates of

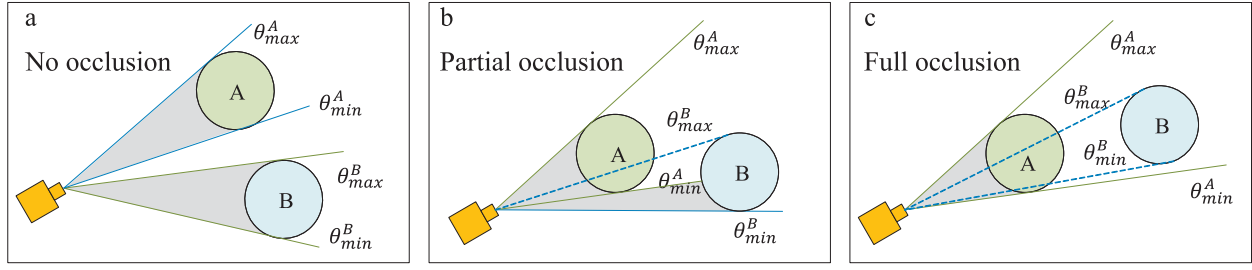


Fig. 16. Illustration of the calculation of visible areas (gray areas) and the determination of occlusion situations. (a) No occlusion. (b) Partial occlusion. (c) Full occlusion.

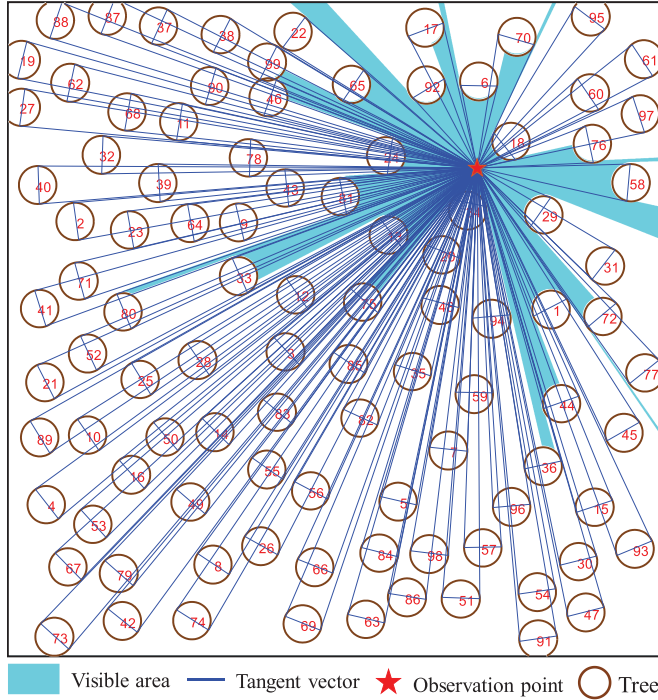


Fig. 17. Illustration of visibility analysis based on the 2-D simplification of trees.

the intersection point of circle B can be derived by

$$\begin{cases} (x - O_{ocx})^2 + (y - O_{ocy})^2 = r^2 \\ \frac{x - O_{ocx}}{T_x - O_{ocx}} = \frac{y - O_{ocy}}{T_y - O_{ocy}} \\ \operatorname{argmin}((I_x - O_{ocx})^2 + (I_y - O_{ocy})^2) \end{cases} \quad (\text{A4})$$

where the subscripts ocx and ocy mean the x - y coordinates of the center of the partially occluded circle B. T_x and T_y refer to the x - y coordinates of a tangent point of circle A. I_x and I_y represent the x - y coordinates of the intersection point.

- 4) Mapping of the visible area. Each group of points (one observation point and two endpoints of the visible arc; black dots for a circle in Fig. 16) is connected to create a visible area (gray areas in Fig. 16). Fig. 17 illustrates an example of the visible area map (visibility map).

ACKNOWLEDGMENT

The authors greatly appreciate the group launching the international terrestrial laser scanning (TLS) benchmarking project for kindly providing a public data set of six forest plots. They also sincerely thank the two anonymous reviewers for their insightful and valuable comments and suggestions, which have greatly improved their algorithm and presentation and strengthened the research depth of this work.

REFERENCES

- [1] M. Disney, "Terrestrial LiDAR: A three-dimensional revolution in how we look at trees," *New Phytologist*, vol. 222, no. 4, pp. 1736–1741, Jun. 2019.
- [2] X. Liang *et al.*, "Terrestrial laser scanning in forest inventories," *ISPRS J. Photogramm. Remote Sens.*, vol. 115, pp. 63–77, May 2016.
- [3] P. Wilkes *et al.*, "Data acquisition considerations for terrestrial laser scanning of forest plots," *Remote Sens. Environ.*, vol. 196, pp. 140–153, Jul. 2017.
- [4] K. Calders *et al.*, "Realistic forest stand reconstruction from terrestrial LiDAR for radiative transfer modelling," *Remote Sens.*, vol. 10, no. 6, p. 933, Jun. 2018.
- [5] A. E. L. Stovall, A. G. Vorster, R. S. Anderson, P. H. Evangelista, and H. H. Shugart, "Non-destructive aboveground biomass estimation of coniferous trees using terrestrial LiDAR," *Remote Sens. Environ.*, vol. 200, pp. 31–42, Oct. 2017.
- [6] F. Hosoi and K. Omasa, "Voxel-based 3-D modeling of individual trees for estimating leaf area density using high-resolution portable scanning LiDAR," *IEEE Trans. Geosci. Remote Sens.*, vol. 44, no. 12, pp. 3610–3618, Dec. 2006.
- [7] R. Hu *et al.*, "Estimating the leaf area of an individual tree in urban areas using terrestrial laser scanner and path length distribution model," *ISPRS J. Photogramm. Remote Sens.*, vol. 144, pp. 357–368, Oct. 2018.
- [8] J. Chave *et al.*, "Ground data are essential for biomass remote sensing missions," *Surv. Geophys.*, vol. 40, pp. 1–18, Apr. 2019.
- [9] S. Soudarissanane, R. Lindenbergh, M. Menenti, and P. Teunissen, "Scanning geometry: Influencing factor on the quality of terrestrial laser scanning points," *ISPRS J. Photogramm. Remote Sens.*, vol. 66, no. 4, pp. 389–399, Jul. 2011.
- [10] J. Trochta, K. Král, D. Janík, and D. Adam, "Arrangement of terrestrial laser scanner positions for area-wide stem mapping of natural forests," *Can. J. Forest Res.*, vol. 43, no. 4, pp. 355–363, Apr. 2013.
- [11] M. Béland, J.-L. Widłowski, R. A. Fournier, J.-F. Côté, and M. M. Verstraete, "Estimating leaf area distribution in savanna trees from terrestrial LiDAR measurements," *Agricult. Forest Meteorol.*, vol. 151, no. 9, pp. 1252–1266, Sep. 2011.
- [12] J. L. Lovell, D. L. B. Jupp, G. J. Newnham, and D. S. Culvenor, "Measuring tree stem diameters using intensity profiles from ground-based scanning LiDAR from a fixed viewpoint," *ISPRS J. Photogramm. Remote Sens.*, vol. 66, no. 1, pp. 46–55, Jan. 2011.
- [13] T. Yun *et al.*, "Simulation of multi-platform LiDAR for assessing total leaf area in tree crowns," *Agricult. Forest Meteorol.*, vols. 276–277, Oct. 2019, Art. no. 107610.
- [14] X. Liang, P. Litkey, J. Hyyppä, H. Kaartinen, M. Vastaranta, and M. Holopainen, "Automatic stem mapping using single-scan terrestrial laser scanning," *IEEE Trans. Geosci. Remote Sens.*, vol. 50, no. 2, pp. 661–670, Feb. 2012.

- [15] P. Wan, T. Wang, W. Zhang, X. Liang, A. K. Skidmore, and G. Yan, "Quantification of occlusions influencing the tree stem curve retrieving from single-scan terrestrial laser scanning data," *Forest Ecosyst.*, vol. 6, no. 1, p. 43, Dec. 2019.
- [16] D. V. D. Zande, I. Jonckheere, J. Stuckens, W. W. Verstraeten, and P. Coppin, "Sampling design of ground-based LiDAR measurements of forest canopy structure and its effect on shadowing," *Can. J. Remote Sens.*, vol. 34, no. 6, pp. 526–538, Dec. 2008.
- [17] Y. Chen *et al.*, "Estimation of forest leaf area index using terrestrial laser scanning data and path length distribution model in open-canopy forests," *Agricult. Forest Meteorol.*, vol. 263, pp. 323–333, Dec. 2018.
- [18] C. Gollob, T. Ritter, C. Wassermann, and A. Nothdurft, "Influence of scanner position and plot size on the accuracy of tree detection and diameter estimation using terrestrial laser scanning on forest inventory plots," *Remote Sens.*, vol. 11, no. 13, p. 1602, Jul. 2019.
- [19] M. J. Ducey and R. Astrup, "Adjusting for nondetection in forest inventories derived from terrestrial laser scanning," *Can. J. Remote Sens.*, vol. 39, no. 5, pp. 410–425, 2013.
- [20] W. Zhang, Y. Chen, H. Wang, M. Chen, X. Wang, and G. Yan, "Efficient registration of terrestrial LiDAR scans using a coarse-to-fine strategy for forestry applications," *Agricult. Forest Meteorol.*, vol. 225, pp. 8–23, Sep. 2016.
- [21] K. Olofsson and H. Olsson, "Estimating tree stem density and diameter distribution in single-scan terrestrial laser measurements of field plots: A simulation study," *Scandin. J. Forest Res.*, vol. 33, no. 4, pp. 365–377, May 2018.
- [22] W. Dai, B. Yang, Z. Dong, and A. Shaker, "A new method for 3D individual tree extraction using multispectral airborne LiDAR point clouds," *ISPRS J. Photogramm. Remote Sens.*, vol. 144, pp. 400–411, Oct. 2018.
- [23] M. Mohan *et al.*, "Individual tree detection from unmanned aerial vehicle (UAV) derived canopy height model in an open canopy mixed conifer forest," *Forests*, vol. 8, no. 9, p. 340, Sep. 2017.
- [24] M. Kuronen, H. M. Henttonen, and M. Myllymäki, "Correcting for non-detection in estimating forest characteristics from single-scan terrestrial laser measurements," *Can. J. Forest Res.*, vol. 49, no. 1, pp. 96–103, Jan. 2019.
- [25] M. Zasada, K. Stereńczak, W. M. Dudek, and A. Rybski, "Horizon visibility and accuracy of stocking determination on circular sample plots using automated remote measurement techniques," *Forest Ecol. Manage.*, vol. 302, pp. 171–177, Aug. 2013.
- [26] D. O'Sullivan and A. Turner, "Visibility graphs and landscape visibility analysis," *Int. J. Geograph. Inf. Sci.*, vol. 15, no. 3, pp. 221–237, Apr. 2001.
- [27] X. Liang *et al.*, "International benchmarking of terrestrial laser scanning approaches for forest inventories," *ISPRS J. Photogramm. Remote Sens.*, vol. 144, pp. 137–179, Oct. 2018.
- [28] S. Bechtold and B. Höfle, "HELIOS: A multi-purpose LiDAR simulation framework for research, planning and training of laser scanning operations with airborne, ground-based mobile and stationary platforms," *ISPRS Ann. Photogramm., Remote Sens. Spatial Inf. Sci.*, vol. 3, no. 3, pp. 161–168, 2016.
- [29] F. D. Schneider, D. Kükenbrink, M. E. Schaepman, D. S. Schimel, and F. Morsdorf, "Quantifying 3D structure and occlusion in dense tropical and temperate forests using close-range LiDAR," *Agricult. Forest Meteorol.*, vol. 268, pp. 249–257, Apr. 2019.
- [30] V. Pratt, "Direct least-squares fitting of algebraic surfaces," *ACM SIG-GRAPH Comput. Graph.*, vol. 21, no. 4, pp. 145–152, Aug. 1987.
- [31] J. Trochta, M. Kruček, T. Vrška, and K. Král, "3D forest: An application for descriptions of three-dimensional forest structures using terrestrial LiDAR," *PLoS ONE*, vol. 12, no. 5, May 2017, Art. no. e0176871.
- [32] W. Zhang *et al.*, "A novel approach for the detection of standing tree stems from plot-level terrestrial laser scanning data," *Remote Sens.*, vol. 11, no. 2, p. 211, Jan. 2019.
- [33] D. Seidel and C. Ammer, "Efficient measurements of basal area in short rotation forests based on terrestrial laser scanning under special consideration of shadowing," *iForest-Biogeosciences Forestry*, vol. 7, no. 4, pp. 227–232, Aug. 2014.
- [34] R. Astrup, M. J. Ducey, A. Granhus, T. Ritter, and N. von Lüpke, "Approaches for estimating stand-level volume using terrestrial laser scanning in a single-scan mode," *Can. J. Forest Res.*, vol. 44, no. 6, pp. 666–676, Jun. 2014.
- [35] M. G. Wing, A. Eklund, and L. D. Kellogg, "Consumer-grade global positioning system (GPS) accuracy and reliability," *J. Forestry*, vol. 103, no. 4, pp. 169–173, Jun. 2005.
- [36] E. Naesset and T. Jonmeister, "Assessing point accuracy of DGPS under forest canopy before data acquisition, in the field and after postprocessing," *Scandin. J. Forest Res.*, vol. 17, no. 4, pp. 351–358, Jan. 2002.
- [37] M. Wulder, K. O. Niemann, and D. G. Goodenough, "Local maximum filtering for the extraction of tree locations and basal area from high spatial resolution imagery," *Remote Sens. Environ.*, vol. 73, no. 1, pp. 103–114, Jul. 2000.
- [38] H. Kaartinen *et al.*, "An international comparison of individual tree detection and extraction using airborne laser scanning," *Remote Sens.*, vol. 4, no. 4, pp. 950–974, Mar. 2012.
- [39] L. Li *et al.*, "Quantifying understory and overstory vegetation cover using UAV-based RGB imagery in forest plantation," *Remote Sens.*, vol. 12, no. 2, p. 298, Jan. 2020.



Linyuan Li (Associate Member, IEEE) received the Ph.D. degree from Beijing Normal University, Beijing, China, in 2020.

He was a Joint Ph.D. Student with the EMMAH Unit, Institut National de la Recherche Agronomique (INRA), Avignon, France, from 2017 to 2019. His research interests include unmanned aerial vehicle (UAV)-based remote sensing of vegetation, multi-angular remote sensing, and light detection and ranging (LiDAR) data processing.



Xihan Mu received the Ph.D. degree in remote sensing from the School of Geography, Beijing Normal University, Beijing, China, in 2009.

He is with the State Key Laboratory of Remote Sensing Science, Institute of Remote Sensing Science and Engineering, Faculty of Geographical Science, Beijing Normal University. His research interests focus on multi-angular remote sensing, especially in the retrieval/measurement of vegetation structural parameters.



Maxime Soma received the M.S. degree in forestry, agronomy and ecosystems management (sp. forests and their environment) from AgroParisTech, Nancy, France, in 2015 and the Ph.D. degree from the University of Aix-Marseille, Marseille, France, and French Institute for Agricultural Research (INRA), Paris, France, in 2019.

From 2016 to 2019, he worked with the Mediterranean Forest Research Unit at INRA on terrestrial light detection and ranging (LiDAR) data processing for forests biomass and 3-D structure measurements.

He is currently a Post-Doctoral Researcher with INRA in Mediterranean Environment and Modelling of Agroecosystems Lab and works on the use of LiDAR instruments for crops monitoring.



Peng Wan received the M.S. degree in survey engineering from Henan Polytechnic University, Jiaozuo, China, in 2015 and the Ph.D. degree in remote sensing from Beijing Normal University, Beijing, China, in 2019.

He is a Researcher with the Changjiang River Scientific Research Institute (CRSRI), Wuhan, China. His research interests include point cloud processing, visualization of 3-D geometric information, and remote sensing of vegetation and water.



Jianbo Qi received the Ph.D. degree from Beijing Normal University, Beijing, China, in 2019. He was a Joint Ph.D. Student with CESBIO, Paul Sabatier University, Toulouse, France, from 2016 to 2018. He is an Assistant Professor with Beijing Forestry University, Beijing. His research interests include 3-D radiative transfer modeling, realistic forest scene simulation, and vegetation parameter retrieval.



Wuming Zhang received the Ph.D. degree from Tsinghua University, Beijing, China, in 2004. He was a Professor with the State Key Laboratory of Remote Sensing Science, Faculty of Geographical Science, Beijing Normal University, Beijing. He is a Professor with Sun Yat-sen University, Guangzhou, China. His main research interests are photogrammetry and remote sensing, especially light detection and ranging (LiDAR) point cloud processing and applications.



Yiyi Tong received the B.S. degree in physical geography from Beijing Normal University, Beijing, China, in 2017, where she is pursuing the master's degree. Her research interests include the estimation of radiation budgets and the validation of remote sensing models in rugged terrains.



Ronghai Hu received the Ph.D. degree in remote sensing from Beijing Normal University, Beijing, China, and ICube Laboratory, Centre National de la Recherche Scientifique (CNRS), University of Strasbourg, Strasbourg, France, in 2018. He is a Lecturer with the College of Resources and Environment, University of Chinese Academy of Sciences, Beijing. His research interests include indirect measurement and airborne retrieval of leaf area index (LAI), remote sensing of vegetation, light detection and ranging (LiDAR), and scale effect on remote sensing.



Guangjian Yan (Senior Member, IEEE) received the Ph.D. degree from the Institute of Remote Sensing Applications, Chinese Academy of Sciences, Beijing, China, in 1999. He is a Professor with the State Key Laboratory of Remote Sensing Science, Faculty of Geographical Science, Beijing Normal University, Beijing. He has authored more than 200 articles. His research interests include multiangular remote sensing, vegetation remote sensing, scale issues, and radiation budget.